Journal of Energy Chemistry 85 (2023) 164–180

Contents lists available at ScienceDirect

Journal of Energy Chemistry

journal homepage: www.elsevier.com/locate/jechem

http://www.journals.elsevier.com/journal-of-energy-chemistry/

A versatile strategy to activate self-sacrificial templated Li_2MnO_3 by defect engineering toward advanced lithium storage

Jian-En Zhou [a,1], Yanhua Peng [a,1], Xiaoyan Sang [b], Chunlei Wu [c], Yiqing Liu [a], Zhijian Peng [a], Hong Ou [a], Yongbo Wu [d], Xiaoming Lin [a,*], Yuepeng Cai [a,*]

[a] Guangzhou Key Laboratory of Materials for Energy Conversion and Storage, Joint Laboratory of Energy and Materials Chemistry (South China Normal University-Guangzhou Tianci New Materials Co., Ltd.), Key Laboratory of Theoretical Chemistry of Environment, Ministry of Education, School of Chemistry, South China Normal University, Guangzhou 510006, Guangdong, China

[b] National Engineering Research Center for Carbohydrate Synthesis, Key Lab of Fluorine and Silicon for Energy Materials and Chemistry of Ministry of Education, Jiangxi Normal University, Nanchang 330022, Jiangxi, China

[c] Guangzhou Huifu Research Institute Co., Ltd, Nanxiang San Lu, Guangzhou 510663, Guangdong, China

[d] Guangdong Provincial Key Laboratory of Quantum Engineering and Quantum Materials, National Demonstration Center for Experimental Physics Education, School of Physics and Telecommunication Engineering, South China Normal University, Guangzhou 510006, Guangdong, China

ARTICLE INFO

Article history:
Received 14 April 2023
Revised 11 May 2023
Accepted 14 May 2023
Available online 26 May 2023

Keywords:
Li_2MnO_3
Metal-organic framework
Oxygen vacancy
Lithium-ion battery
Electrochemical activity

ABSTRACT

Despite the dazzling theoretical capacity, the devasting electrochemical activity of Li_2MnO_3 (LMO) caused by the difficult oxidation of Mn^{4+} impedes its practical application as the lithium-ion battery (LIB) cathode. The efficacious activation of the Li_2MnO_3 by importing electrochemically active Mn^{3+} ions or morphological engineering is instrumental to its lithium storage activity and structural integrity upon cycling. Herein, we propose a conceptual strategy with metal-organic frameworks (MOFs) as self-sacrificial templates to prepare oxygen-deficient Li_2MnO_3 (O_v-LMO) for exalted lithium storage performance. Attributed to optimized morphological features, LMO materials derived from Mn-BDC (H_2BDC = 1,4-dicarboxybenzene) delivered superior cycling/rate performances compared with their counterparts derived from Mn-BTC (H_3BTC = 1,3,5-benzenetricarboxylicacid) and Mn-PTC (H_4PTC = pyromellitic acid). Both experimental and theoretical studies elucidate the efficacious activation of primitive LMO materials toward advanced lithium storage by importing oxygen deficiencies. Impressively, O_v-LMO derived from Mn-BDC (O_v-BDC-LMO) delivered intriguing reversible capacities (179.2 mA h g^{-1} at 20 mA g^{-1} after 200 cycles and 100.1 mA h g^{-1} at 80 mA g^{-1} after 300 cycles), which can be attributed to the small particle size that shortens pathways for Li^+/electron transport, the enhanced redox activity induced by abundant oxygen vacancies, and the optimized electronic configuration that contributes to the faster lithium diffusivity. This work provides insights into the rational design of LMO by morphological and atomic modulation to direct its activation and practical application as an advanced LIB cathode.

1. Introduction

Lithium-ion batteries (LIBs) have become indispensable electrochemical energy storage and conversion devices due to their remarkable power density, satisfying cyclability, negligible memory effect, and environmental friendliness since the emergence of the intensified energy crisis caused by the dwindling fossil fuel [1]. Nevertheless, the development of the next-generation LIBs is bottlenecked by the dissatisfying electrochemical properties of the prevailing electrode materials. Following this, the exploration of high-performance cathodes and the innovation in cathode technology become prerequisites for advanced LIBs, since cathode materials are crucial for the overall performance of LIB systems [2,3]. Relentless endeavors have been devoted to the modification and design of cathode materials for exalting electrochemical properties during recent decades.

Owing to the enticing theoretical capacities that can better meet the future requirements of battery endurance, Li-rich layered materials have been extensively studied. Among them, Li_2MnO_3

* Corresponding authors.
E-mail addresses: linxm@scnu.edu.cn (X. Lin), caiyp@scnu.edu.cn (Y. Cai).
[1] These authors contributed equally to this work.

https://doi.org/10.1016/j.jechem.2023.05.014

(LMO) has been regarded as a promising alternative for the mercantile LIB cathode materials such as $LiCoO_2$ (LCO), $Li[Ni_xCo_yMn_{1-x-y}]O_2$ (NCM), and $LiFePO_4$ (LFP) due to its superiority in theoretical capacity (460, 274, ~280, and ~170 mA h g^{-1} for LMO, LCO, NCM, and LFP, respectively) [4,5]. Despite the dazzling potential to be utilized as a high-capacity LIB cathode, the practical application of LMO is hampered by the electrochemical inactivity related to the untoward oxidation of Mn^{4+} (less than 50 mA h g^{-1} for LMO microparticles) and safety hazards (huge irreversible capacity loss of ~130 mA h g^{-1} above 4.5 V) related to fatal O_2 emission [6]. To tackle these obstacles, extensive efforts have been dedicated to the effectual activation and the optimized morphological and microstructural properties of LMO. Hitherto, several strategies have been applied to LMO to suppress structural degradation, exalt electrochemical activity, and enhance electronic conductivity, such as partial doping with other transition metal atoms, surface/interface modification, morphology control, nanorization, microstructural manipulation, construction of multiphase materials, utilization of conductive matrices/networks, and so on [7–10]. Among these strategies, morphological and microstructural regulations are promising methodologies to promote lithium storage activity and extend cyclability on the premise of ensuring battery energy density.

It is widely substantiated and acknowledged that morphological features are crucial metrics in LIB electrode design and can be facilely adjusted by synthetic routes. The morphology-performance relationship has been extensively probed to excavate the possibility of resolving the inherently unsatisfactory electrochemical performance of LMO. For instance, nano-sized LMO materials pronouncedly outperformed their micro-sized opponents in the previous reports [6,11], which verified the undisputed impact of particle size on the electrochemical performance of LMO. Surface properties and particle stability are vital to mechanical robustness and structural integrity during repetitive cycles [12,13], whose improvement is beneficial to mitigating pernicious structural collapse. In addition, the amplified surface area and the well-developed porosity are conducive to increasing active sites and multidimensional diffusion pathways [14]. For better integration and utilization of the above morphological advantages, it is viable to explore suitable self-sacrificial templates to directionally fabricate LMO materials with desirable structures, among which metal-organic frameworks (MOFs) have become prevalent self-sacrificial templates for energy material engineering due to their flexible designability and omnifarious morphologies [15]. The enticing properties of MOFs render them the ideal templates for the compositional and structural design during LIB cathode (e.g. Li-rich metal oxides, polyanionic composites, metal sulfides, and metal fluorides) development [16], thereby indicating the possibility and practicability of MOF-templated strategy for controllable synthesis of LMO.

Apart from morphology control, the atomic structure and electronic configuration can significantly tune the electrochemical behaviors of LMO materials. Pristine LMO is confronted with the intrinsic undesirable electrochemical activity caused by the improbable oxidation of Mn^{4+} and the dissatisfying cycling durability caused by the phase transition and oxygen shearing during activation [17,18]. To ameliorate the redox activity and cope with the structural degradation, the oxygen-deficient strategy has been extensively investigated and utilized to regulate the electrochemical properties of LMO at the atomic level. Reductants such as metal hydrides [19], sodium tetrahydroborate ($NaBH_4$) [20], and stearic acid [21] can efficaciously introduce oxygen defects by capturing lattice oxygen to generate proper amounts of Mn^{3+}, by which extra electrochemical activities can be accessed. Owing to the enhanced redox kinetics caused by the appropriate concentration of Mn^{3+}, boosted ion migration related to enlarged lattice space, and suppressed oxygen shearing leading to detrimental structural change, the as-reported oxygen vacancy-enriched LMO materials display expected superiority in lithium storage with superior reversible capacity, pronouncedly higher initial Coulombic efficiency, exalted rate capability, and prolonged cycle life [14,19,20], henceforth indicating the effectiveness of the oxygen-deficient strategy in LMO cathode modification.

Inspired by these research advances, we systematically develop a multifunctional synthetic protocol to integrate the MOF-templated method and oxygen-deficient strategy for optimizing morphological and atomic structure. The 1,4-dicarboxybenzene-, 1,3,5-benzenetricarboxylicacid-, and pyromellitic acid-based Mn-MOFs (abbreviated as Mn-BDC, Mn-BTC, and Mn-PTC, respectively) were synthesized by solvothermal reaction and were later utilized as self-sacrificial templates to fabricate LMO (denoted as BDC-LMO, BTC-LMO, and PTC-LMO, respectively) by solid-state conversion. Afterward, stearic acid was employed as the reductant to prepare the oxygen vacancy-enriched LMO (denoted as O_v-BDC-LMO, O_v-BTC-LMO, and O_v-PTC-LMO, respectively). Experimentally, O_v-BDC-LMO outperforms its counterparts in electrochemical properties with an elevated specific capacity, boosted ion/electronic conductivity, and remarkable multiplier performance due to the optimized morphological and electronic features. The theoretical study also verifies the enticing advantages of O_v-LMO including amended lattice configuration, manipulated electronic structure, enhanced electrical conductivity, energetically favorable delithiation, and expedited Li^+ migration, which further expounds the plausibility of experimental results. This work envisions a versatile strategy to maximize the complementarity of auspicious morphological features retained from MOF precursors and the oxygen vacancies facilitating electrochemical activation toward efficacious modification of LMO for high-performance LIB application.

2. Experimental

2.1. Material preparation

The Mn-MOFs with carboxyl-based ligands were prepared by solvothermal reactions according to the previous study [22,23]. $Mn(CH_3COO)_2{\cdot}4H_2O$ (1 mmol) was dissolved in 6 mL of *N,N*-dimethylformamide (DMF)/methanol (V_D: V_m = 5:1) hybrid solvent to obtain solution **A**, which was repeated three times. H_2BDC (1 mmol), H_3BTC (1 mmol), and H_4PTC (1 mmol) were dissolved in 30 mL of DMF/methanol (V_D: V_m = 5:1) to obtain solutions **B**, **C**, and **D**, respectively. Afterward, solution **A** was slowly poured into solutions **B**, **C**, and **D**, separately, and the mixed solutions were stirred at room temperature for 5 h, and then transferred into a 50 mL Teflon-lined stainless-steel autoclave and heated at 140 °C for 24 h. After being cooled down to room temperature, the MOF was collected by centrifugation with a rotating speed of 10,000 r min^{-1} and washed three times thoroughly with methanol. Finally, the products were dried in an oven at 60 °C for 12 h to obtain the Mn-MOFs powder with H_2BDC, H_3BTC, and H_4PTC as organic ligands (denoted as Mn-BDC, Mn-BTC, and Mn-PTC, respectively).

The LMO materials without oxygen vacancy were fabricated via pyrolysis of the Mn-MOF templates with Li_2CO_3 as the Li source with a molar ratio of Li: Mn = 2.05:1. The dried MOFs were mixed with Li_2CO_3 by ball-milling and then calcined at 800 °C for 8 h with a ramping rate of 5 °C min^{-1} in air. Finally, the LMO materials without oxygen vacancy derived from Mn-BDC, Mn-BTC, and Mn-PTC were obtained (denoted as BDC-LMO, BTC-LMO, and PTC-LMO, respectively). To prepare the oxygen-deficient samples (denoted as O_v-BDC-LMO, O_v-BTC-LMO, and O_v-PTC-LMO, respectively), BDC-LMO, BTC-LMO, and PTC-LMO were calcinated at 340 °C for

8 h after mixing with stearic acid with a molar ratio of 20:1 in N_2 according to the prior report [21].

2.2. Material characterization

The crystallographic data and phase analyses of the Mn-MOFs and LMO materials were implemented with an X-ray diffraction spectrophotometer (XRD, Ultima IV, Japan) using Cu K_α radiation with a scanning rate of 10° min^{-1} between 10° and 90°. Thermogravimetric analysis (TGA, STA-409PC, Germany) was measured with an air flow of 10 mL min^{-1} and a ramping rate of 10 °C min^{-1}. The elemental configuration and interactions of LMO materials were detected using Raman spectroscopy (Renishaw inVia, UK) with a wavenumber scale of 50–2000 cm^{-1} using excitation light of 532 nm with an argon ion laser beam. The valence state and compositions of the particles were evaluated by X-ray photoelectron spectroscopy (XPS, Thermo Scientific *K*-Alpha$^+$, USA). The electron paramagnetic resonance (EPR) test was conducted at an amplitude of 2 G, a modulation frequency of 100 kHz, and a sweep width of 100 G for 80 s under a dark condition (JES FA200, Japan). The Brunauer-Emmett-Teller (BET) was implemented using an ASAP 2046 surface area and pore size analyzer (USA) at liquid nitrogen temperature (77 K). The morphologies and particle sizes of the obtained samples were analyzed with the field emission scanning electron microscope (FESEM, FEI Quanta 250 FEG, USA) and transmission electron microscopy (TEM, FEI Talos F200X, USA) with an energy-dispersive spectroscopy (EDS) system.

2.3. Electrochemical measurement

Electrochemical measurements of LMO were investigated using CR2032 coin cells. The cathode electrodes were prepared by using as-prepared LMO, acetylene black, and polyvinylidene fluoride (PVDF) with a weight ratio of 7:2:1 dispersed in *N*-methyl-2-pyrrolidone (NMP). Afterward, the slurry was coated onto aluminum foil and dried at 110 °C, while the electrodes were prepared as ~12 mm disks with a mass load of active materials of ~1.0 mg. In the half-cell system, the metallic Li, Celgard 2400, and a solution with 1 M $LiPF_6$ in ethylene carbonate (EC), diethyl carbonate (DEC), and ethyl methyl carbonate (EMC) (the volume ratio of 1:1:1) were used as the counter electrode, separator, and electrolyte, respectively. The coin cells were assembled in an argon-filled glove box (H_2O < 0.1 ppm, O_2 < 0.1 ppm). The charge/discharge performances were performed by a battery test system (Land CT 2001A, China) between 2.0 and 4.8 V (vs. Li/Li$^+$) at 40 mA g^{-1} and 25 °C. The rate capabilities were assessed with the cell charged/discharged at multiple current densities of 0.2, 0.4, 1, 2, and 5 C (1 C = 200 mA h g^{-1}). The long cycling experiments of the LMO materials were evaluated at 25 °C using a charge-discharge rate of 80 mA g^{-1}. The cyclic voltammogram (CV) curves were measured from 2.0 to 4.8 V at scan rates of 0.2, 0.4, 0.6, 0.8, and 1.0 mV s^{-1} using an electrochemical workstation (CHI-660E, China). The electrochemical impedance spectroscopy (EIS) was estimated with an alternating current (AC) amplitude of 5 mV in the frequency ranging from 100 kHz to 0.01 Hz at room temperature. The galvanostatic intermittent titration technique (GITT) measurement was carried out to investigate the diffusion coefficient of lithium ions after 2 cycles for activation of the fresh coin cell at the current density of 20 mA g^{-1}, during which the cell was alternately discharged/charged for 4 min coupled with rest intervals of 1.0 h.

2.4. Theoretical study

All the spin-polarized (AFM) density functional theoretical (DFT) calculations were conducted based on the Vienna Ab-inito Simulation Package (VASP) [24]. The electron-ion interactions were described by the Projected Augmented-Wave (PAW) potentials, while the exchange-correlation interactions were calculated by employing the Perdew-Burke-Enzerhof (PBE) pseudopotentials of Generalized Gradient Approximation (GGA) with a Hubbard *U* extension (*U* value) of 3.9 eV for Mn [25,26]. The vdW-D3 method developed by Grimme was employed to describe the van der Waals interaction [27]. The plane-wave energy cutoff was set to 450 eV. The convergence threshold was set to 1.0×10^{-5} eV in energy and 0.02 eV per Angstrom in force. The Brillouin zone was modeled by the gamma-centered Monkhorst-Pack scheme, in which a $5 \times 3 \times 5$ grid was adopted for LMO and O_v-LMO. The CINEB method was applied to compute the Li atom diffusion energy barrier.

3. Results and discussion

3.1. Structural and morphological properties

The synthetic procedure of O_v-LMO materials via solvothermal reaction, solid-state lithiation at high temperature, and low-temperature reduction is schematically illustrated in Fig. 1(a). The high phase purity and crystallinity of Mn-BDC, Mn-BTC, and Mn-PTC were examined by the XRD patterns, as depicted in Fig. S1(a). Simultaneously, the TGA measurement was conducted to investigate the pyrolysis temperatures of the MOF precursors, which indicates that MOF precursors are entirely decomposed at 450–600 °C (Fig. S1b). The MOF precursors were meticulously calcined at 800 °C with Li_2CO_3 as the Li source according to the TGA results to guarantee the high crystallinity of the LMO products [28,29]. Afterward, the O_v-LMO products were prepared by calcination of LMO and stearic acid at a lower temperature of 340 °C.

Powder XRD characterization was utilized to estimate the crystallographic configuration of LMO and O_v-LMO derived from Mn-BDC, Mn-BTC, and Mn-PTC. The XRD patterns of (O_v-)BDC-LMO (Fig. 1b), (O_v-)BTC-LMO (Fig. 1e), and (O_v-)PTC-LMO (Fig. 1h) present visible characteristic diffraction peaks at 18.7°, 20.8°, 21.7°, 37.0°, 44.8°, 48.8°, 58.9°, 64.5°, and 65.5° affirmatively correlating to the (0 0 1), (0 2 0), (1 1 0), (1 3 0), (1 3 1), (−1 3 2), (1 3 2), (−1 3 3), and (−3 3 1) facets, respectively, in the Li_2MnO_3 phase with a *C*2/*m* space group (JCPDS No. 84-1634) [30]. It is worth noting that there are significant variations in XRD patterns due to the existence of oxygen vacancies. Fig. S2 exhibits the (0 0 1) facets of the LMO and O_v-LMO samples, in which the diffraction peaks of the O_v-LMO samples slightly shift to lower diffraction angles, indicating the enlarged *d*-spacing induced by the oxygen vacancies [21]. Additionally, Rietveld refinements were employed to further evaluate the impact of oxygen vacancies on crystallographic features. The R_{wp} values of O_v-BDC-LMO (Fig. 1c), BDC-LMO (Fig. 1d), O_v-BTC-LMO (Fig. 1f), BTC-LMO (Fig. 1g), O_v-PTC-LMO (Fig. 1i), and PTC-LMO (Fig. 1j) can be determined to be 4.53%, 5.36%, 5.99%, 5.13%, 5.17%, and 6.18%, respectively, elucidating good agreement factors for all samples. As shown in Table S1, the O_v-LMO materials display larger lattice parameters compared with the LMO materials due to the shared O atoms brought by oxygen vacancies [31]. The Rietveld refinement results suggest that oxygen occupancy values of O_v-BDC-LMO, O_v-BTC-LMO, and O_v-BTC-LMO are 0.927, 0.937, and 0.961, respectively, as tabulated in Table S2. Hence, the concentration of oxygen vacancies in O_v-BDC-LMO, O_v-BTC-LMO, and O_v-BTC-LMO can be determined to be 7.3%, 6.3%, and 3.9%, respectively, according to oxygen occupancy [32]. These results not only verify the successful generation of oxygen vacancies but also unravel the different lattice structures of LMO and O_v-LMO samples.

The Raman spectra were conducted to evaluate and compare the structural characteristics of LMO and O_v-LMO. As delivered in Fig. 2(a–c), the strong characteristic peaks at the high-frequency

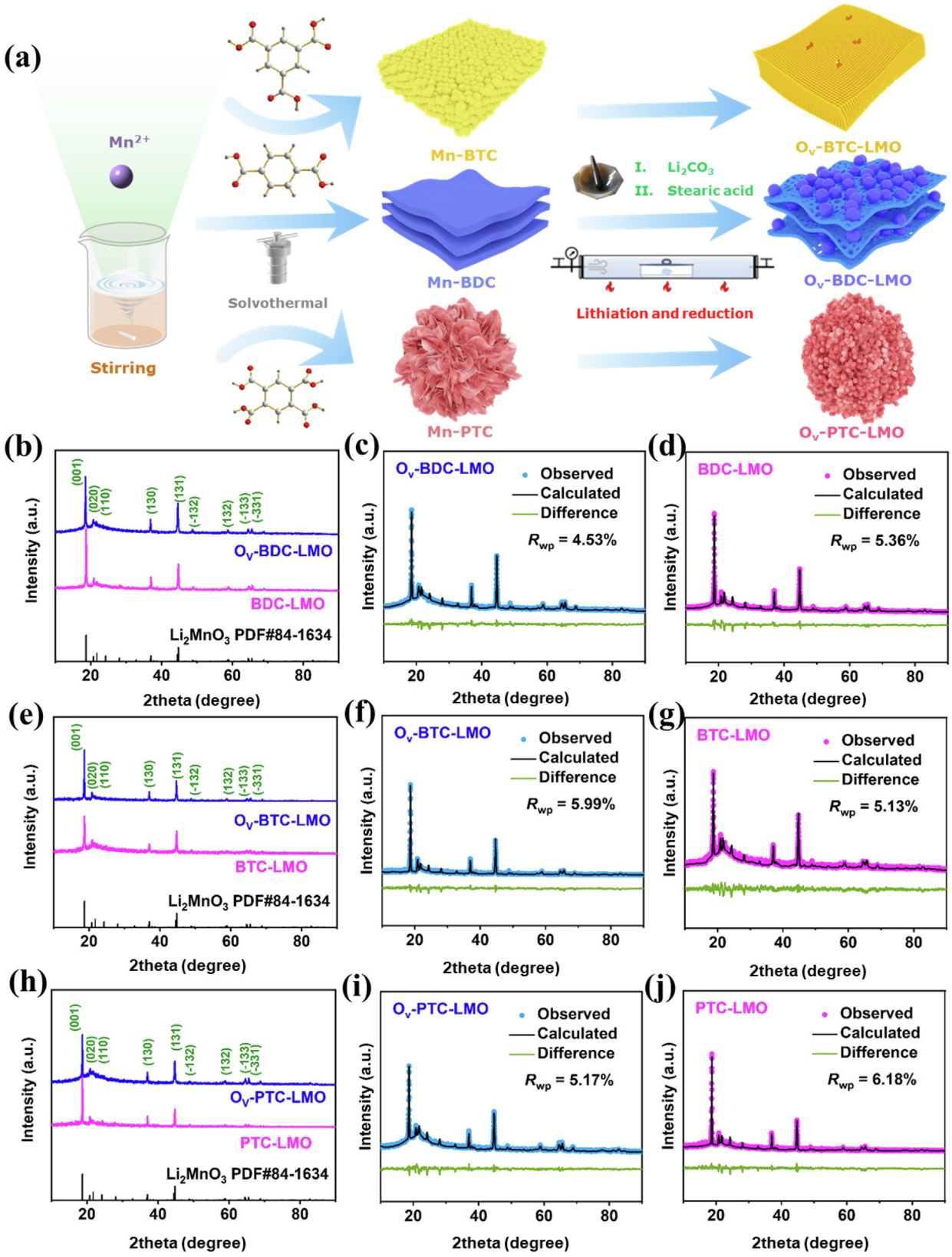

Fig. 1. (a) The synthetic procedure of O_v-BDC-LMO, O_v-BTC-LMO, and O_v-PTC-LMO. XRD patterns of (b) (O_v-)BDC-LMO, (e) (O_v-)BTC-LMO, and (h) (O_v-)PTC-LMO. Rietveld refinements of (c) O_v-BDC-LMO, (d) BDC-LMO, (f) O_v-BTC-LMO, (g) BTC-LMO, (i) O_v-PTC-LMO, and (j) PTC-LMO.

region and the ones at the low-frequency region are related to the Mn—O and Li—O bonds, respectively, manifesting the high purity of all samples [20]. The Raman peak intensities of O_v-LMO are profoundly lower than those of LMO, which can be ascribed to the enhanced conductivity caused by the oxygen vacancies [33]. Notably, the Raman peak intensity ratios of the characteristic peaks

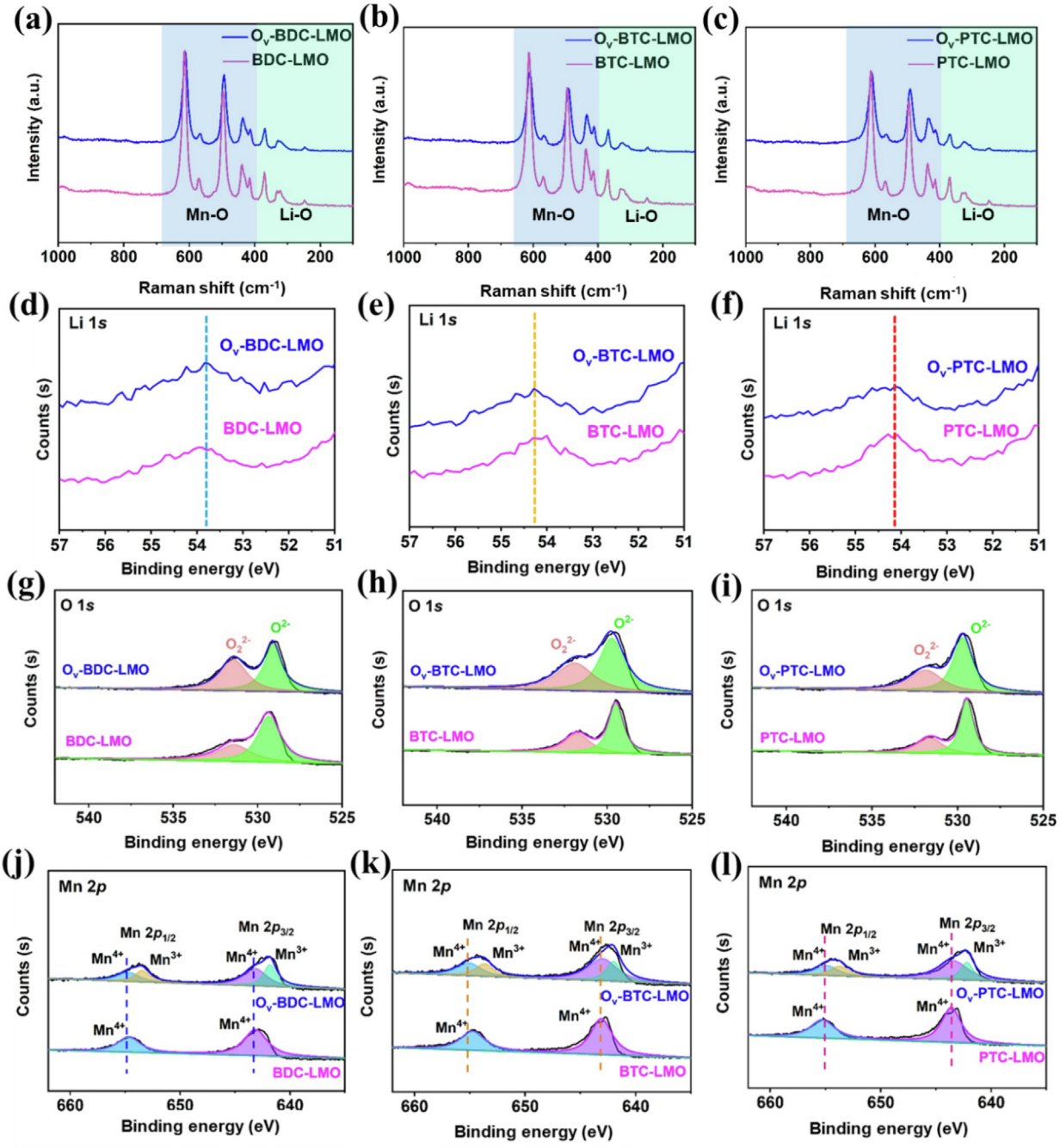

Fig. 2. (a–c) The panoramic Raman spectra and the high-resolution XPS spectra of (d–f) Li 1*s*, (g–i) O 1*s*, and (j–l) Mn 2*p* for (O_v-)BDC-LMO, (O_v-)BTC-LMO, and (O_v-)PTC-LMO, respectively.

centered at ~610 and ~500 cm^{-1} increase with the existence of oxygen vacancies (1.34, 1.67, 1.35, 1.54, 1.29, and 1.52 for BDC-LMO, O_v-BDC-LMO, BTC-LMO, O_v-BTC-LMO, PTC-LMO, and O_v-PTC-LMO, respectively), among which the peaks at ~610 cm^{-1} slightly shift toward the lower wave-number side with the emergence of shoulder peaks at ~630 cm^{-1} (Fig. S3a–c). These phenomena can be attributed to the strengthened Mn—O bonds and the formation of spinel-structure domains in O_v-LMO [11,20]. To efficaciously confirm the oxygen-deficient texture, EPR measurements were performed for LMO and O_v-LMO, during which the characteristics of both Mn^{4+} and oxygen vacancies can be identified. As expected, O_v-BDC-LMO (Fig. S3d), O_v-BTC-LMO (Fig. S3e), and O_v-PTC-LMO (Fig. S3f) jointly show broad Lorentzian (g = 1.998) and additional sharp (g = 2.003) signals compared with their counterparts without oxygen vacancy, corresponding to the unpaired electrons of Mn^{4+} and the typical feature of oxygen vacancies, respectively [21,34], which is in conformity with the XRD refinement and Raman results and can well elucidate the electronic property that is effectively manipulated by oxygen vacancies.

XPS measurements were implemented to elucidate the compositional features and chemical states in LMO and O_v-LMO materials. The survey-scan XPS spectra reveal the coexistence of Li, Mn, and O in all samples, in which the C 1*s* signal at 284.8 eV was utilized to calibrate the binding energy (Fig. S4a–c). As presented in Fig. 2(d–f), the high-resolution Li 1*s* spectra verify the successful lithiation of Mn-MOFs by the as-proposed solid-state conversion

strategy. The core-level O 1*s* spectra can be deconvoluted into 2 sub-peaks located at 531.8 and 529.3 eV (Fig. 2g–i), correlating to the surficial absorbed and lattice oxygen, respectively, whose intensity ratios (0.73, 0.69, 0.52, 0.41, 0.39, and 0.37 for O_v-BDC-LMO, O_v-BTC-LMO, O_v-PTC-LMO, BDC-LMO, BTC-LMO, and PTC-LMO, respectively) can be distinctly enhanced by oxygen vacancies [20,21]. The lattice oxygen trait is assignable to the O^{2-} in the Li_2MnO_3 lattice, while the surficial absorbed oxygen signal originates from the highly reactive peroxo-like (O_2^{2-}) oxygen radicals [35,36]. Moreover, the oxygen defects (the ones on the surface and sub-surface particularly) can significantly change the local environment of oxygen in LMO materials and trigger the formation of unbonded structure, thereby facilitating the generation of highly reactive O_2^{2-} radicals and hence resulting in the enhanced O_2^{2-} peak intensities [35]. According to the valence neutrality, Mn shows a single valence of 4+ in LMO and mixture valences of 3+ and 4+ in O_v-LMO. As expected, there are four deconvoluted peaks in the high-resolution Mn 2*p* spectra of O_v-BDC-LMO (Fig. 2j), O_v-BTC-LMO (Fig. 2k), and O_v-PTC-LMO (Fig. 2l), among which the characteristic peaks centered at 654.7 and 643.2 eV are attributed to Mn^{4+} ions, while the ones centered at 653.3 and 641.8 eV are related to Mn^{3+} ions [29]. To further estimate the valence states of Mn, the high-resolution XPS spectra of Mn 3*s* of (O_v-)BDC-LMO (Fig. S4d), (O_v-)BTC-LMO (Fig. S4e), and (O_v-)PTC-LMO (Fig. S4f) are enclosed to calculate the average oxidation state (AOS). The AOS value can be assessed by the formula: $AOS = 8.956 - 1.126\Delta E$, where ΔE represents the splitting energy between binding energies of the main peak and its satellite [20,32], by which the AOS values of O_v-BDC-LMO, O_v-BTC-LMO, and O_v-PTC-LMO can be estimated to be +3.55, +3.66, and +3.78, respectively. In contrast, the chemical valence of the Mn element in the oxygen vacancy-free samples can be calculated to be 4.00 according to the above formula, which is in line with the deconvoluted results of the core-level Mn 2*p* spectrum. These results suggest that the concentration of oxygen defects can significantly manipulate the oxidation states of metal ions.

The morphological features and architecture of the MOF precursors, LMO, and O_v-LMO were systematically analyzed by SEM and TEM characterizations. The SEM image of the Mn-BDC precursor (Fig. 3a) features a spongy lamellar architecture, where this superstructure was found to be well retained in the derived BDC-LMO (Fig. 3b) and O_v-BDC-LMO (Fig. 3c) products. Simultaneously, the BDC-LMO and O_v-BDC-LMO products display a secondary structure composed of small particles with a diameter of 50–200 nm. As delivered in Fig. 3(d), the Mn-BTC precursor features a staggered coral-like architecture elaborately composed of numerous nanoparticles. The panoramic coral-like morphology is inherited by the BTC-LMO (Fig. 3e) and O_v-BTC-LMO (Fig. 3f) products, but the secondary particles show larger sizes (80–500 nm) and are dispersedly scattered on the primary structure. Additionally, the Mn-PTC precursor bears a flower-like morphology constructed with numerous thin films, as depicted in Fig. 3(g). The PTC-LMO (Fig. 3h) and O_v-PTC-LMO (Fig. 3i) maintain the flower-like parent architecture with thicker petal-like bulks densely accumulating on it, which manifests the inferior particle growth. In light of these observations, MOF precursors can be utilized to dexterously manipulate the morphology and particle size of the resultant product due to the competition between the nucleation process and crystal growth [29], and thus the rational selection of monomers can efficaciously modulate the structural properties to realize controllable preparation. The larger steric hindrance tapers the cluster connectivity and hence is unfavorable for crystal growth and formation of magnified pore volume [37], which results in inferior particle formation, less porous architectures, smaller surface area, and lower crystallinity of Mn-BTC- and Mn-PTC-derived samples compared with the ones derived from Mn-BDC. It is of note that the oxygen-deficient samples display slightly smaller particles distributed on the well-retained primary structure, in turn manifesting the negligible destruction of primary particles by the low-temperature reduction [14,38], which ameliorates the surface property, provides abundant active sites, alleviates structural destruction, further enhances the electrochemical activity, and prolongs the cycle life.

Correspondingly, the N_2 physisorption isotherms were acquired at 77 K to further demonstrate the porous traits, as elaborated in Fig. S5(a). The BET surface areas of O_v-BDC-LMO, O_v-BTC-LMO, and O_v-PTC-LMO were found to be 246.57, 226.71, and 96.86 $m^2 g^{-1}$, respectively. The pore size distribution curves are exhibited in Fig. S5(b), in which O_v-BDC-LMO displays superior total pore volume compared with its counterparts. The pore sizes of O_v-BDC-LMO are scattered at 1.7–61.2 nm, while the ones of O_v-BTC-LMO and O_v-PTC-LMO are scattered in the range of 1.8–88.9 and 3.4–53.7 nm, respectively, in turn, manifesting the hierarchical micro-meso-macro mode for O_v-BDC-LMO and O_v-BTC-LMO as well as the meso-macro mode for O_v-PTC-LMO. The superior porosity is propitious to suppress volume variation, increase active sites, extend diffusion aisles, and enrich surface/interface defects, thereby favoring the diffusion kinetics and pseudocapacitive contribution [39,40]. Interestingly, preliminary characterizations jointly expound the higher oxygen defect concentration of O_v-BDC-LMO than O_v-BTC-LMO and O_v-PTC-LMO, which is related to the morphological feature and particle size. Size and morphology effects can synergistically influence the resultant O_v concentration, during which smaller particle radius and larger surface area can afford more vacancy-acceptable sites and hence promote the O_v formation [41,42], and thus the resultant architectures derived from parent MOFs play a critical role in O_v levels. Bestowed by the enlarged surface area and extended vacancy-accepting layer, more oxygen defects can be generated in the BDC-derived samples during the low-temperature reduction procedure.

To further unveil the internal architectures of the LMO and O_v-LMO products, the TEM technique was adopted. As disclosed by the TEM images, BDC-LMO (Fig. 4a) and O_v-BDC-LMO (Fig. 4d) feature a layered architecture composed of film-like secondary particles with a diameter of 50–200 nm, which conforms to the SEM characterization. As expected, Fig. 4(b and e) displays the structural peculiarity of BTC-LMO and O_v-BTC-LMO with a larger particle diameter, while Fig. 4(c and f) demonstrates the larger particle size of PTC-LMO and O_v-PTC-LMO. The high-resolution TEM (HRTEM) images of BDC-LMO (Fig. 4g), BTC-LMO (Fig. 4h), PTC-LMO (Fig. 4i), O_v-BDC-LMO (Fig. 4j), O_v-BTC-LMO (Fig. 4k), and O_v-PTC-LMO (Fig. 4l) profoundly record the conspicuous lattice fringes correlating to the (001) facets of the Li_2MnO_3 phase. Among them, the oxygen-deficient samples exhibit amplified interplanar distances and more distinct lattice distortion, indicating the crystal disarrangements and enlarged lattice parameters induced by the oxygen vacancies [21,43]. Correspondingly, the selected area electron diffraction (SAED) patterns of BDC-LMO (Fig. 4m), BTC-LMO (Fig. 4n), PTC-LMO (Fig. 4o), O_v-BDC-LMO (Fig. 4p), O_v-BTC-LMO (Fig. 4q), and O_v-PTC-LMO (Fig. 4r) jointly feature the polycrystalline diffraction rings indexed to the representative (001), (130), and (131) facets of the monoclinic Li_2MnO_3, indicating the satisfying phase purity. In addition, high-angle annular dark-field scanning TEM (HAADF-STEM) and corresponding element mappings of BDC-LMO (Fig. 4s), BTC-LMO (Fig. 4t), PTC-LMO (Fig. 4u), O_v-BDC-LMO (Fig. 4v), O_v-BTC-LMO (Fig. 4w), and O_v-PTC-LMO (Fig. 4x) illustrate the homogeneous distribution of Mn and O. As mentioned above, the oxygen-deficient texture promotes the formation of lattice distortion, which is related to the atomic rearrangement and the derived regional spinel regimes throughout the holistic layered structure [14,19,44,45]. As a result, Mn^{3+} ions can exist stably in the Li_2MnO_{3-x} lattice by manipulating the atomic configuration and local structure with the integration of

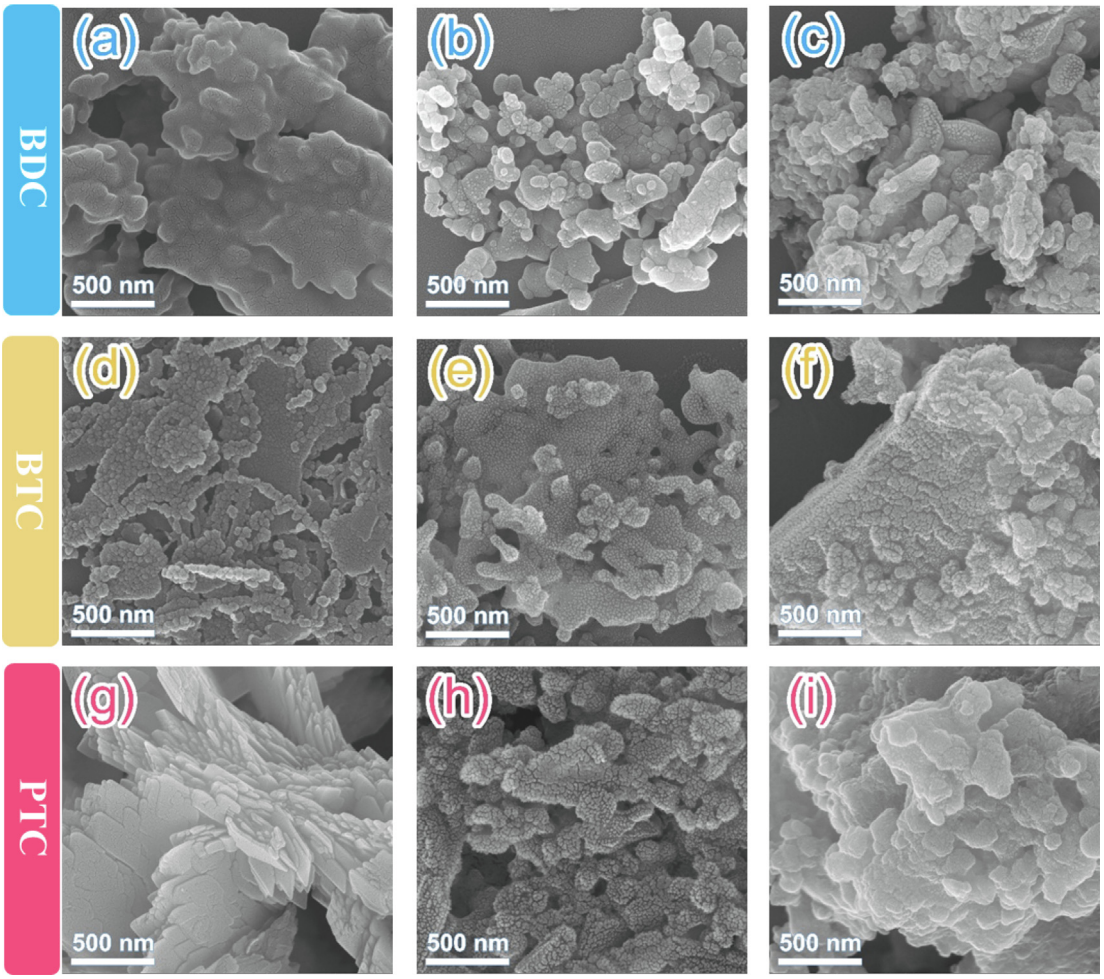

Fig. 3. The SEM images of (a) Mn-BDC, (b) BDC-LMO, (c) O_v-BDC-LMO, (d) Mn-BTC, (e) BTC-LMO, (f) O_v-BTC-LMO, (g) Mn-PTC, (h) PTC-LMO, and (i) O_v-PTC-LMO.

the predominant layered structure and minority spinel domain. To support this assumption from the atomic level, the spherical aberration-corrected HAADF-STEM and spherical aberration-corrected annular bright-field STEM(ABF-STEM) images are disclosed in Fig. 5, in which the oxygen-deficient samples exhibit spinel regimes in the layered bulk, thereby elucidating the local structure changes triggered by oxygen deficiencies [46,47]. The HAADF-STEM images can effectively visualize the cations, by which the different traits of layered and spinel structures can be identified with the arrangement of bright dots. LMO materials present a typical $C2/m$ space group, while both majority $C2/m$ and minority $Fd\bar{3}m$ features appear in O_v-LMO materials, thereby revealing the layered-spinel integrated structure induced by oxygen vacancies. Considering the insensitivity of HAADF-STEM to oxygen, ABF-STEM images were employed to visualize the oxygen vacancies in the lattice structures, in which the oxygen positions appearing brighter indicate oxygen vacancies. As expected, oxygen deficiencies can be detected in the O_v-LMO materials, while complete oxygen occupancies are available in the LMO counterparts. All these material characterization results verify the successful synthesis of the target products and the efficacious introduction of oxygen vacancies.

3.2. Electrochemical properties

The electrochemical properties of LMO and O_v-LMO were comprehensively studied to illustrate the efficaciousness of the oxygen-deficient strategy for the activation and optimization of Li_2MnO_3 as an advanced LIB cathode. O_v-BDC-LMO (Fig. 6a), O_v-BTC-LMO (Fig. 6b), and O_v-PTC-LMO (Fig. 6c) samples exhibit reversible capacities of 179.2, 117.0, and 97.5 mA h g^{-1}, respectively, at 20 mA g^{-1} after 200 cycles, overperforming their counterparts without oxygen vacancies (103.2, 62.4, and 17.3 mA h g^{-1} for BDC-LMO, BTC-LMO, and PTC-LMO, respectively). All samples bear prominent capacity increase and large capacity fluctuation over the initial 100 loops, the initial 50 cycles particularly, which can be attributed to the activation process through the phase transformation with the generation of the spinel phase in the layered superstructure [48]. After the entire activation, it is noteworthy that all cathode materials underwent a capacity attenuation, which can be ascribed to the irreversible oxygen shearing and structural degradation upon repetitive (de)lithiation processes [17,49], resulting in inverted U-shaped cycling profiles for (O_v-)LMO samples. Profiting from the facilitated activation induced by the oxygen-deficient nature, suppressed oxygen extraction, and mitigated adverse phase destruction, the O_v-LMO samples present superior lithium storage capability, enhanced reversibility, and prolonged cycle life.

As expected, the O_v-LMO samples feature superiority in rate performance compared with their counterparts without oxygen vacancy (Fig. 6d–f). Superior reversible capacities are presented by O_v-BDC-LMO (199.5, 187.9, 167.2, 136.0, and 105.8 mA h g^{-1} at 0.1, 0.2, 0.4, 1, and 2 C, respectively), O_v-BTC-LMO (118.7, 112.9, 109.8, 81.4, and 62.0 mA h g^{-1} at 0.1, 0.2, 0.4, 1, and 2 C,

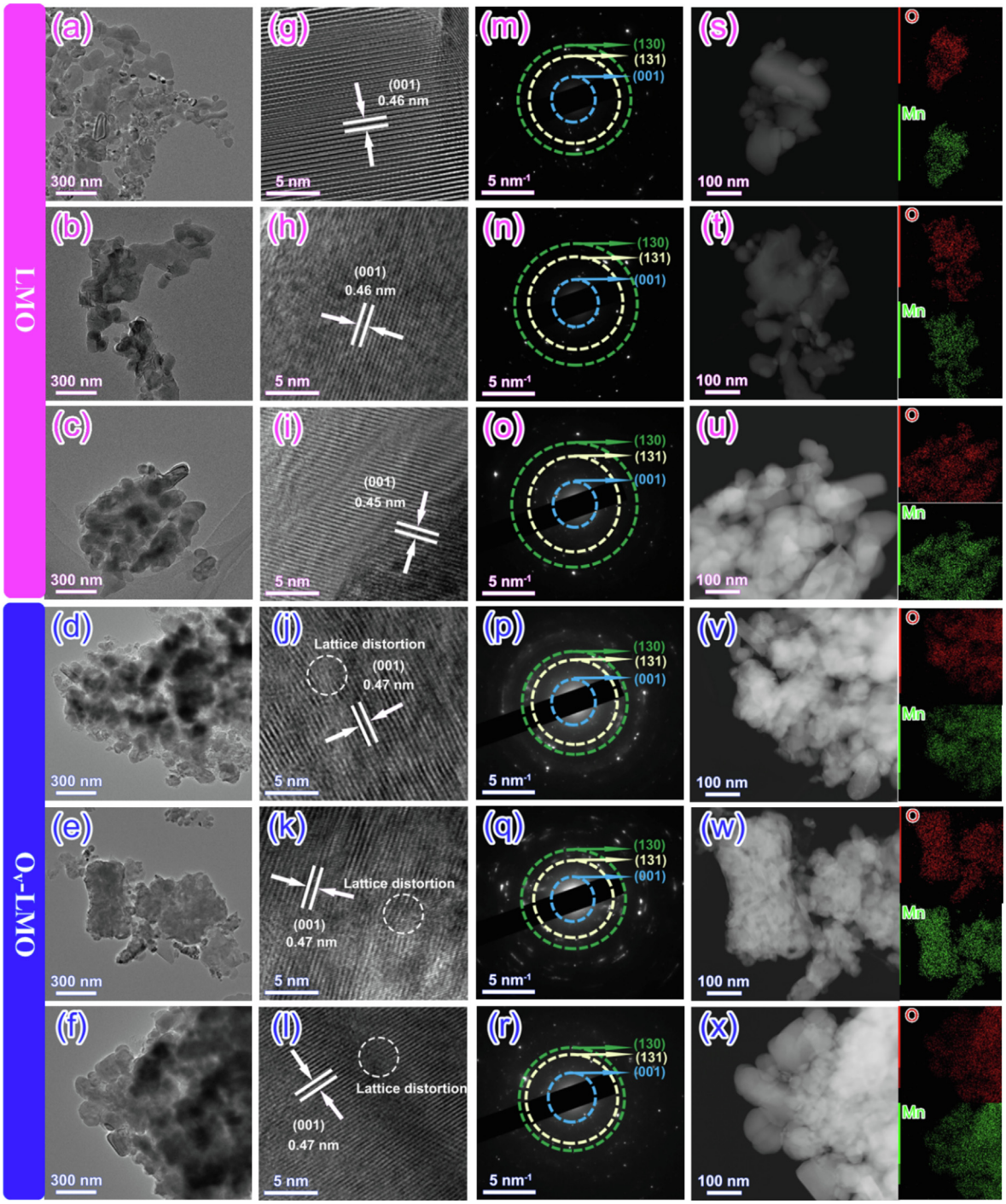

Fig. 4. (a–f) TEM images, (g–l) HRTEM images, (m–r) SAED patterns, and (s–x) HAADF-STEM images and corresponding element mappings of BDC-LMO, BTC-LMO, PTC-LMO, O_v-BDC-LMO, O_v-BTC-LMO, and O_v-PTC-LMO, respectively.

respectively), and O_v-PTC-LMO (110.4, 97.6, 80.7, 57.8, and 39.5 mA h g^{-1} at 0.1, 0.2, 0.4, 1, and 2 C, respectively) at different current densities. In contrast, BDC-LMO (96.2, 76.3, 63.2, 43.4, and 37.9 mA h g^{-1} at 0.1, 0.2, 0.4, 1, and 2 C, respectively), BTC-LMO (80.2, 71.9, 63.8, 50.1, and 39.4 mA h g^{-1} at 0.1, 0.2, 0.4, 1, and 2 C, respectively), and PTC-LMO (71.4, 65.9, 50.5, 27.1, and 13.1 mA h g^{-1} at 0.1, 0.2, 0.4, 1, and 2 C, respectively) deliver subpar rate capabilities due to their inferior electrochemical activity. Most samples deliver remarkable reversibility when the current density rebounds to 0.1 C, among which O_v-BDC-LMO displays a stable discharge capacity of 218.9 mA h g^{-1} surpassing the capacities of other samples (198.9, 124.3, 116.2, 53.9, and 45.5 mA h g^{-1} for O_v-BTC-LMO, O_v-PTC-LMO, BDC-LMO, BTC-LMO, and PTC-LMO, respectively) after the rate recovery. It is noteworthy that the Mn-BDC-derived samples outperform their counterparts derived from Mn-BTC and Mn-PTC in both cycling durability and rate capability, which is endowed with the rational selection of organic ligands improving particle growth and the optimized morphological features favoring the structural integrity during cycling [12,29]. As a supplement to the above deduction, the long-term cycling performances of O_v-BDC-LMO, O_v-BTC-LMO, and O_v-PTC-LMO at 0.4 C for 300 loops are presented in Fig. S6, which reveal the superior

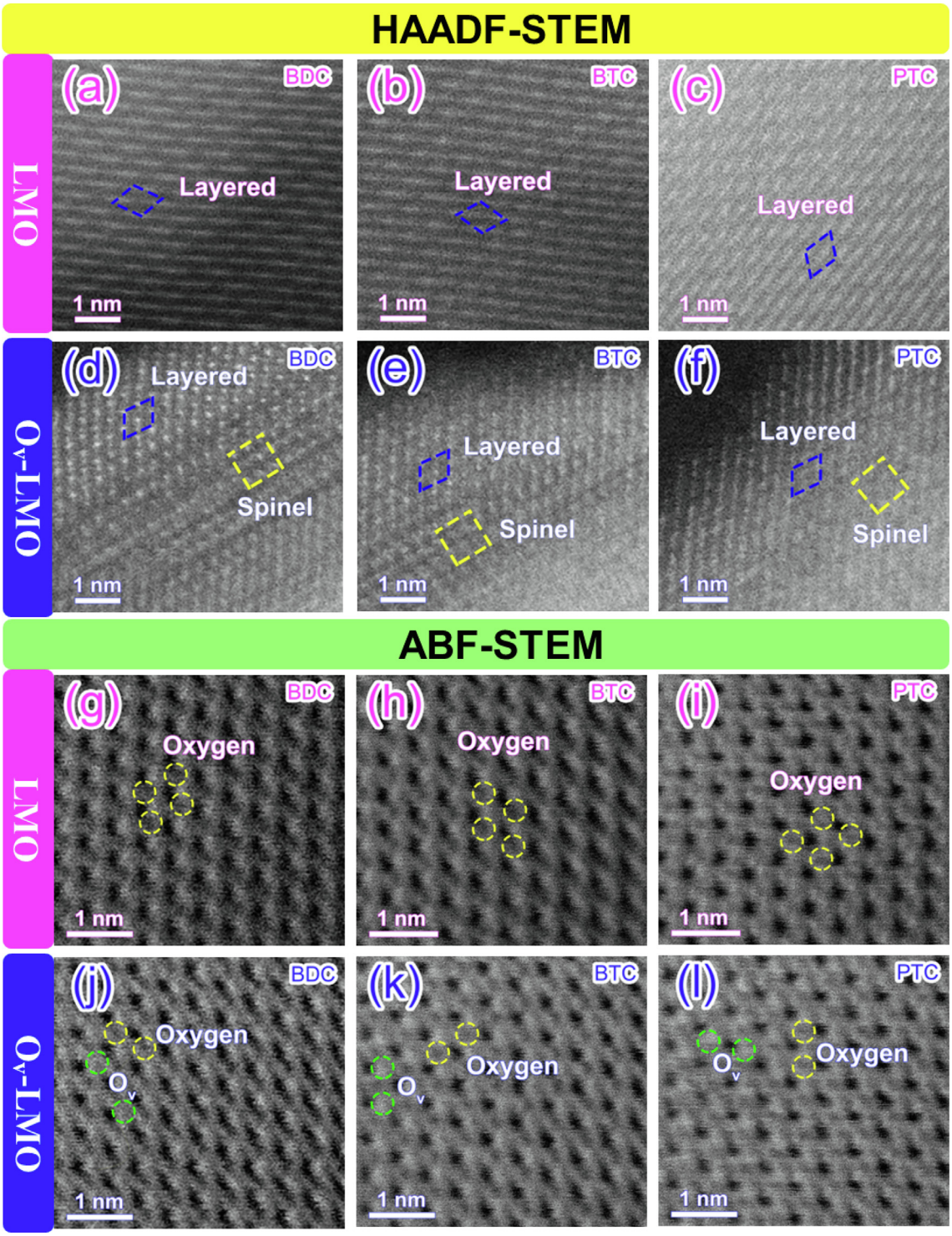

Fig. 5. (a–f) Spherical aberration-corrected HAADF-STEM and (g–l) spherical aberration-corrected ABF-STEM images for BDC-LMO, BTC-LMO, PTC-LMO, O_v-BDC-LMO, O_v-BTC-LMO, and O_v-PTC-LMO, respectively.

cycling durability of O_v-BDC-LMO with a reversible capacity of 100.1 mA h g^{-1} outperforming those of O_v-BTC-LMO (95.5 mA h g^{-1}) and O_v-PTC-LMO (58.9 mA h g^{-1}). Moreover, the cross-sectional SEM images are disclosed in Fig. S7 to embody the alleviated volumetric fluctuation of the oxygen-deficient and the Mn-BDC-derived samples, further unraveling the exalted electrochemical performance induced by the optimized morphological and microstructural properties.

The galvanostatic charge/discharge (GCD) profiles of all samples performed at 20 mA g^{-1} were recorded to better demonstrate the working mechanism of the activation process of LMO and O_v-LMO electrodes. As depicted in Fig. 6(g–i) and Fig. S8(a–c), O_v-BDC-LMO, O_v-BTC-LMO, and O_v-PTC-LMO display superior initial Coulombic efficiency (ICE) of 68.6%, 62.7%, and 63.3%, respectively, while BDC-LMO, BTC-LMO, and PTC-LMO distinctly lag behind their oxygen-deficient counterparts with ICE of 34.2%, 39.9%, and

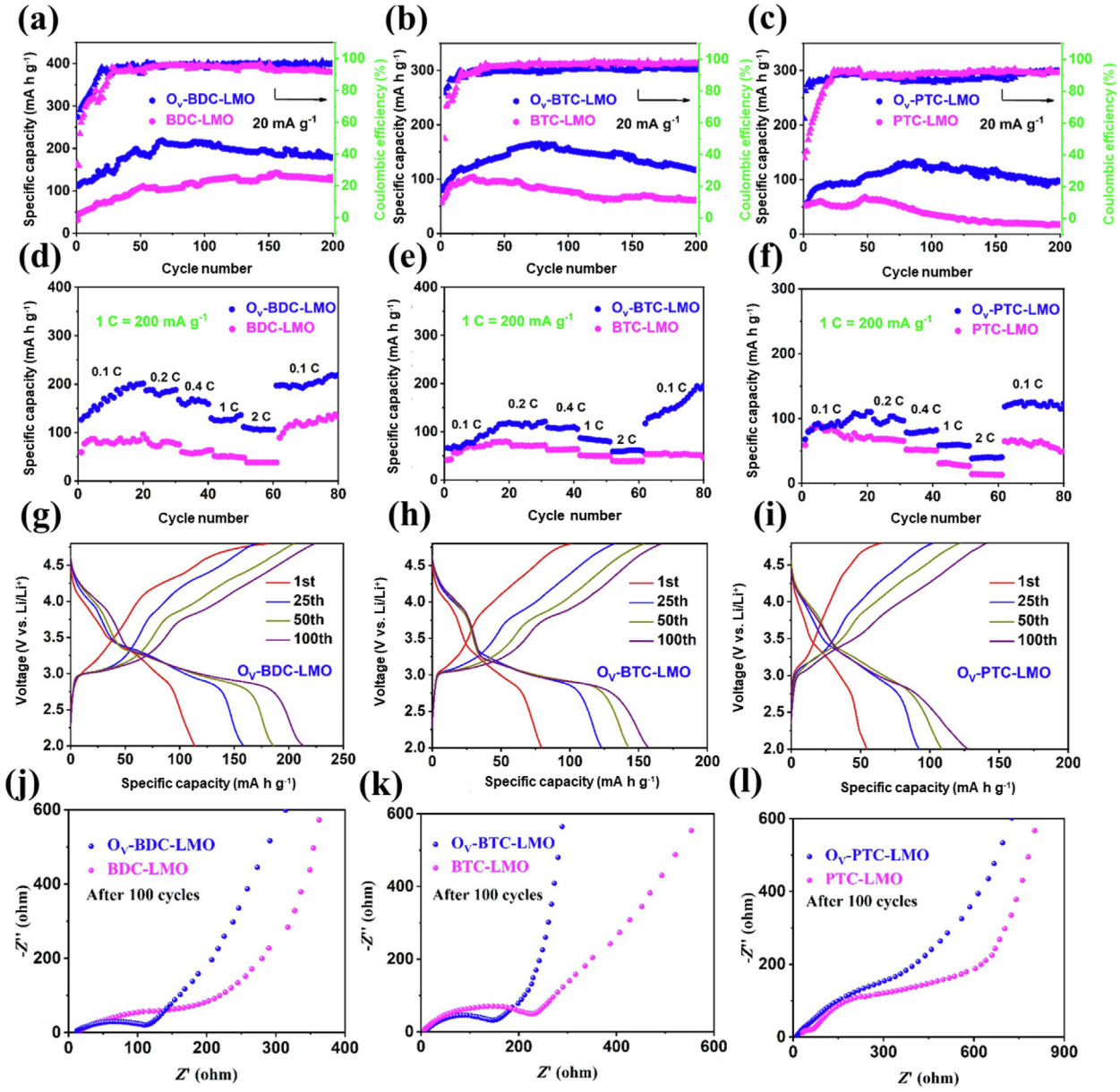

Fig. 6. The cycling performance at 20 mA g^{-1} for 200 loops of (a) (O_v-)BDC-LMO, (b) (O_v-)BTC-LMO, and (c) (O_v-)PTC-LMO. The rate performance at 0.1, 0.2, 0.4, 1, and 2 C (1 C = 200 mA g^{-1}) of (d) (O_v-)BDC-LMO, (e) (O_v-)BTC-LMO, and (f) (O_v-)PTC-LMO. The GCD profiles at the 1st, 25th, 50th, and 100th cycle during the cycling test at 20 mA g^{-1} of (g) O_v-BDC-LMO, (h) O_v-BTC-LMO, and (i) O_v-PTC-LMO. Nyquist plots after 100 cycles at 20 mA g^{-1} for (j) (O_v-)BDC-LMO, (k) (O_v-)BTC-LMO, and (l) (O_v-)PTC-LMO.

38.2%, respectively. Two successive charge plateaus can be observed at ~3.9 and ~4.4 V in the O_v-LMO samples during the first cycle, while merely a long voltage plateau appears above 4.4 V in the LMO samples, which can be ascribed to the structural reconstruction caused by severe oxygen extraction in the LMO phase and the buffering structural rearrangement in the O_v-LMO phase induced by the oxygen-deficient feature [19]. As the (dis) charge proceeds in the following cycle, the CE values of all samples stabilize at ~95%, which illustrates the considerable reversibility of the redox reactions. Similar voltage plateau characteristics can be detected after the first cycle in all samples, revealing the redox couples of O_2^{2-}/O^{2-}, Mn^{4+}/Mn^{3+}, and Mn^{3+}/Mn^{2+} from high to low voltage regions [50,51]. The GCD profiles at different current densities of all samples are also disclosed in Fig. S8(d–i), further testifying to the superiority of O_v-BDC-LMO in rate capability.

Furthermore, to unravel the lithium storage behaviors of all samples during cycling from electronic conductivity and lithium diffusivity, EIS measurements were conducted for better comparison. As illustrated in Fig. S9(a–c) and Fig. 6(j–l), Nyquist plots of all samples before and after cycling can be divided into semicircles at high and middle frequency regions related to the resistance of the solid electrolyte interface (SEI) film or the passivation surface layer (denoted as R_f) and the charge transfer resistance (denoted as R_{ct}), respectively, along with the sloping lines at low frequency representing the Warburg impedance (denoted as W_s) related to Li^+ diffusion [31]. Correspondingly, the equivalent circuit model of these materials is schematically portrayed in Fig. S9(d), in which CPE1 and CPE2 stand for the capacitive contribution of the SEI film and the double layer, respectively, while R_s is the resistance contributed by the solution system [51]. The impedance values of all samples can be determined and documented by the simulation with this equivalent model. As delivered in Table S3, the oxygen-deficient samples deliver smaller resistance values when assembled in fresh cells, indicating the superior electronic conductivity

induced by the oxygen vacancies. The resistance values after 100 cycles were also estimated and compared to further illustrate the enhanced electron/ion conductivity related to the activation process, as tabulated in Table S4. Most samples deliver smaller R_f and R_{ct} values after 100 cycles, which is in line with the increasing capacities during cycling measurements and can be ascribed to the appropriate activation by the optimization of the SEI films and the reconstruction of the electrodes [52]. It is noteworthy that the R_{ct} value of PTC-LMO sharply increases after cycling, which is related to the inferior electrical contact caused by the fatal structural degradation and enlarged particle size [28], corresponding to the drastic capacity attenuation during repetitive cycles.

To further investigate the lithium diffusion kinetics, the formula $D_{Li+} = R^2T^2/(2A^2n^4F^4c^2\sigma^2)$ was applied, where D_{Li+}, R, T, A, n, F, c, and σ symbolize the lithium-ion diffusion coefficient, gas constant, absolute temperature (in K), the area of circular electrodes, the number of electron migration in each mole of the active material, Faraday constant, the molar concentration of Li^+, and the Warburg impedance coefficient calculated by the formula $Z' = R_{ct} + R_s + \sigma\omega^{-1/2}$, respectively [52]. According to the linear relationship between the real resistance and the reciprocal square root of the angular frequency, σ values of these samples can be assessed, by which the D_{Li+} values of O_v-BDC-LMO, O_v-BTC-LMO, O_v-PTC-LMO, BDC-LMO, BTC-LMO, and PTC-LMO before cycling can be further estimated to be 1.44×10^{-15}, 1.20×10^{-15}, 3.00×10^{-16}, 1.19×10^{-15}, 3.79×10^{-16}, and 2.38×10^{-16} $cm^2\ s^{-1}$, respectively (Fig. S10a–c). Correspondingly, the D_{Li+} values after 100 cycles for the above samples can be calculated to be 2.20×10^{-15}, 2.16×10^{-15}, 5.10×10^{-16}, 1.44×10^{-15}, 4.95×10^{-16}, and 1.49×10^{-16} $cm^2\ s^{-1}$, respectively, according to the fitted σ values (Fig. S10d–f). The elevated D_{Li+} values affirm the enhanced lithium diffusivity after cycling, which can be attributed to the favorable kinetics for ion migration triggered by oxygen vacancy doping [53]. Among these samples, PTC-LMO exhibits a reducing D_{Li+} value during cycling that is numerically smaller than that before cycling due to its structural inferiority. The EIS results show that morphological and microstructural manipulation is conducive to distinguished electronic/ion conductivity for enhanced lithium storage capacity and remarkable rate performance.

The CV curves were further studied to unveil the working mechanisms of LMO and O_v-LMO in lithium storage. The CV curves for the initial three cycles of six samples are recorded in Fig. 7(a–f), which differentiate the working mechanisms of LMO and O_v-LMO and further exhibit the superior electrochemical properties of O_v-LMO. Three redox couples located at 3.3/2.8 V, 3.8/4.1 V, and 4.5/4.1 V can be detected in the CV curves of O_v-LMO, which can be assigned to the redox activities of Mn^{3+}/Mn^{2+}, Mn^{4+}/Mn^{3+}, and O_2^{2-}/O^{2-}, respectively [50,54], which conform with the GCD curves. It is of note that the oxidation peaks at ~4 V appear during the first cycle in these CV curves, which is ascribed to the transformation from Mn^{3+} to Mn^{4+}. In contrast, the LMO samples show more conspicuous oxidation peaks at ~4.5 V but hardly show traits of Mn^{4+}/Mn^{3+} during anodic scanning in the first cycle, which can be ascribed to the more severe oxygen extraction from the Li_2MnO_3 lattice and is detrimental to the structural integrity and cycling durability [20,46]. After the first cycle, the Mn^{3+}/Mn^{2+}, Mn^{4+}/Mn^{3+}, and O_2^{2-}/O^{2-} redox couples located at 3.2/2.9 V, 4.2/3.4 V, and 4.6/4.0 V are available, among which the cathodic peaks at 2.9 and 3.4 V show increasing intensities as the cycling extends, elucidating the activation process via transformation from layered to spinel phase [51]. The amplified potential difference and aggravated asymmetry of the Mn^{4+}/Mn^{3+} and O_2^{2-}/O^{2-} redox couples presented by the LMO samples indicate inferior redox reversibility [55], thereby impeding the activation process and intensifying the structural destruction.

The above observations expound the different working mechanisms of the O_v-LMO compared with the primitive materials without oxygen vacancy, particularly during the first cycle. For better understanding, the redox activities at the first (de)lithiation cycle are schematically illustrated. Fig. 7(g) portrays the reversible transformation of Mn^{4+} and Mn^{3+} in O_v-LMO during the first cycle, which can be represented by the significant anodic peaks related to oxidation of Mn^{3+} positioned at ~4 V and the cathodic peaks related to the reduction of Mn^{4+} positioned at ~3.8 V in the CV curves. As displayed in Fig. 7(h), LMO undergoes an oxygen shearing process by the transformation of O^{2-} in the lattice to O_2 and the structural activation by reduction of Mn^{4+} to Mn^{3+} during the first cycle [17], which can be uncovered by the sharp anodic peaks at ~4.6 V and the inconspicuous cathodic peaks at ~3.4 V in the CV curves that can deteriorate the electrochemical performance. Therefore, proper Mn^{3+} levels can resolve the electrochemically inactive Mn^{4+} systems to facilitate the activation of LMO and simultaneously inhibit severe capacity attenuation induced by Jahn-Teller distortion [38]. Profiting from the easy activation process and buffered lattice oxygen loss, the oxygen-deficient nature is propitious to exalt lithium storage activity and extend cycling stability, thereby revealing the effectiveness of the oxygen-deficient strategy.

The quantitation of pseudocapacitive behaviors can be utilized to interpret the electrochemical kinetics, reflect the Li^+ diffusion velocity, and further demonstrate the rate capability of electrode materials [5,52]. With this aim, the CV measurement was also performed at different scan rates from 0.2–1.0 mV s^{-1} to differentiate the diffusion-controlled and pseudocapacitive contributions of O_v-LMO and LMO. As demonstrated in Fig. S11(a–c), the CV profiles of O_v-BDC-LMO, O_v-BTC-LMO, and O_v-PTC-LMO show similar features with increasing current intensities as the sweep rate upgrades, indicating remarkable redox reversibility. The CV profiles of BDC-LMO, BTC-LMO, and PTC-LMO at different scan rates are also recorded in Fig. S11(d–f) for better comparison, in which inferior symmetry and enlarged potential differences are presented, revealing the subpar electrochemical reversibility. To precisely quantify the pseudocapacitive contribution ratio related to non-Faradaic reactions, the power-law relationship of $i = av^b$ and the formula $i = k_1v + k_2v^{1/2}$ can be employed, in which i, v, k_1v, and $k_2v^{1/2}$ represent the peak current, scan rate, pseudocapacitive-dominant current, and diffusion-controlled current, respectively [56,57]. Based on the power-law relationship, the b values of peaks 1–4 for these samples can be determined by logarithmically fitting the peak current intensities against scan rates, as disclosed in Fig. S12(a–f). According to the linear fitting results, the estimated b values of O_v-BDC-LMO (0.954, 0.902, 0.825, and 0.830 for peaks 1–4, respectively), O_v-BTC-LMO (0.949, 0.876, 0.815, and 0.818 for peaks 1–4, respectively), and O_v-PTC-LMO (0.879, 0.867, 0.719, and 0.789 for peaks 1–4, respectively) are distinctly higher than those of BDC-LMO (0.832, 0.643, 0.588, and 0.518 for peaks 1–4, respectively), BTC-LMO (0.829, 0.603, 0.576, and 0.509 for peaks 1–4, respectively), and PTC-LMO (0.824, 0.532, 0.514, and 0.506 for peaks 1–4, respectively). The b value approaching 1 indicates the capacitive-dominant process, while the b value close to 0.5 suggests the diffusion-controlled behavior [56]. Therefore, the fitted results of b values demonstrate the preponderant pseudocapacitive contribution of the O_v-LMO materials compared to their primitive counterparts, thereby accelerating the ion diffusion process for more fabulous rate capability.

Predictably, the O_v-LMO samples (89.8%, 86.6%, and 79.7% for O_v-BDC-LMO, O_v-BTC-LMO, and O_v-PTC-LMO, respectively) hold superior pseudocapacitive contributions compared to their corresponding counterparts (51.9%, 45.2%, and 29.4% for BDC-LMO, BTC-LMO, and PTC-LMO, respectively) at the scan rate of 0.4 mV s^{-1}, as depicted in Fig. 7(i–k) and Fig. S11(g–i), respectively. The pseudocapacitive contribution ratios at other scan rates for all

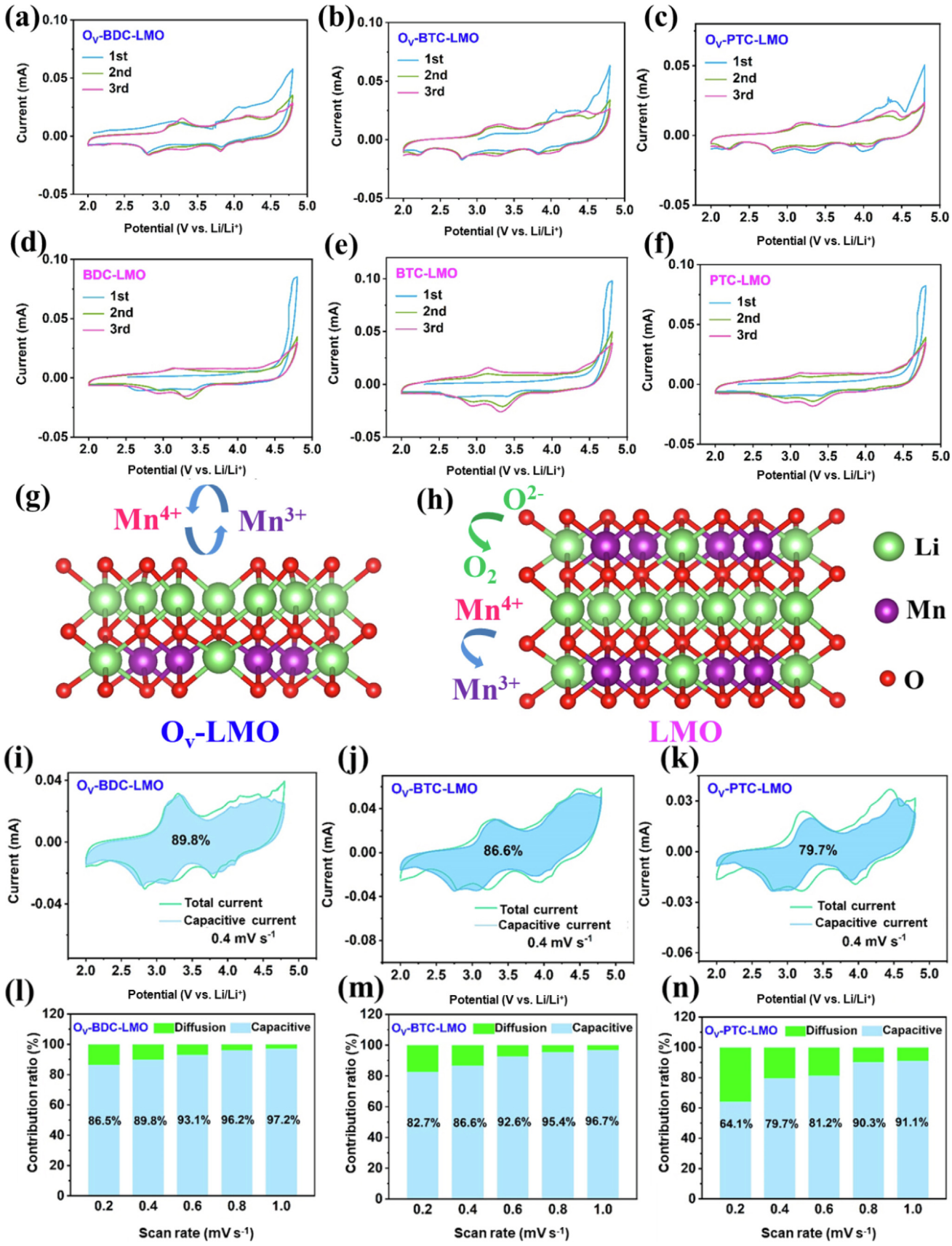

Fig. 7. The CV curves for the first 3 cycles at 0.2 mV s^{-1} for (a) O_v-BDC-LMO, (b) O_v-BTC-LMO, (c) O_v-PTC-LMO, (d) BDC-LMO, (e) BTC-LMO, and (f) PTC-LMO. The schematic illustrations of the first cycle for (g) O_v-LMO and (h) LMO. The separation of the pseudocapacitive contribution at 0.4 mV s^{-1} for (i) O_v-BDC-LMO, (j) O_v-BTC-LMO, and (k) O_v-PTC-LMO. The pseudocapacitive contribution ratios at 0.2–1.0 mV s^{-1} for (l) O_v-BDC-LMO, (m) O_v-BTC-LMO, and (n) O_v-PTC-LMO.

samples are also evaluated, as disclosed in Figs. S13–S18. All samples perform increasing pseudocapacitive-dominant behaviors as the sweep rate upgrades, among which the O_v-LMO samples (Fig. 7l–n) significantly outperform their pristine counterparts (Fig. S11j–l) in pseudocapacitive contribution ratios, which indicates the boosted Li^+ diffusion kinetics induced by oxygen vacancies and is conducive to the distinguished rate performance [57]. In contrast, the diffusion-controlled processes presented by the pristine LMO samples reveal sluggish Li^+ diffusion, thereby leading to the inferiority in electrochemical properties. It is noteworthy that Mn-BDC-derived samples outperform counterparts derived from Mn-BTC and Mn-PTC in pseudocapacitive contributions, which can be ascribed to the optimized morphological feature with larger surface area, more affluent electrochemical active sites, and ameliorated electrode/electrolyte contact [40]. These observations unambiguously verify the strengthened pseudocapacitive behaviors and expedited electrochemical kinetics induced by the integration of morphological and oxygen-deficient effects.

The galvanostatic intermittent titration technique (GITT) measurement was conducted to further support the effectiveness of the oxygen-deficient strategy for exalted lithium diffusivity of LMO materials. The whole-step profiles of GITT titration of O_v-BDC-LMO (Fig. S19a), O_v-BTC-LMO (Fig. S19b), O_v-PTC-LMO (Fig. S19c), BDC-LMO (Fig. S19d), BTC-LMO (Fig. S19e), and PTC-LMO (Fig. S19f) are recorded, in which the voltage fluctuation during relaxation in each titration step stands for the overpotential and indicates the polarization degree [45]. Simultaneously, the lower polarization degree represents the superior lithium diffusivity, which can be quantified by employing the formula $D_{Li+} = \frac{4}{\pi\tau}\left(\frac{m_B V_M}{M_B A}\right)^2\left(\frac{\Delta E_S}{\Delta E_\tau}\right)^2$, where τ, M_B, V_M, m_B, and A symbolize the pulse duration, molecular weight, molar volume, mass load of the active material, and area of the circular electrode, respectively [58,59]. This relationship is schematically demonstrated upon charging, as disclosed in Fig. 8(a–c) and Fig. S19(g–i), corresponding to the voltage response during delithiation processes (Fig. 8d–f and Fig. S20a–c). The above formula is also feasible for the lithiation processes, as depicted in Fig. S20(d–i). Furthermore, the calculated D_{Li+} values during delithiation and lithiation are portrayed in Fig. 8 (g) and Fig. S21, respectively, showcasing the accelerated lithium ion diffusion induced by the oxygen vacancies, which is in line with the pseudocapacitive investigations.

For a better understanding, the working mechanism of the advantageous Li^+ diffusion of the O_v-LMO samples is schematically illustrated in Fig. 8(h) to emphasize the optimized lithium storage behaviors brought by oxygen vacancies. According to the charge neutrality principle, Mn shows a valence of 4+ in the primitive LMO material, which leads to sluggish Li^+ extraction due to the difficult oxidation and electrochemical inactivity of Mn^{4+} [17,47]. Oxygen vacancies are generated after the reduction process to manipulate the valence state in the system, resulting in a higher concentration of Mn^{3+} and the further enhancement of the redox activity for energetically favorable Li^+ extraction and exalted lithium storage capacity [53]. In light of the above analysis, the regulation of the valence state of Mn in the system can favor the redox reaction to reconcile the electrochemical inertness. Other than the boosted redox kinetics, the modulated electronic configuration and the lopsided charge distribution induced by the oxygen defects in the lattice structure are also conducive to the boosted lithium diffusion [34]. Upon delithiation, the presence of oxygen vacancies can lead to positive charge accumulation and promote the formation of positive charge domains, by which the positive electric field-induced Coulomb repulsion facilitates Li^+ extraction to realize the electroneutral state. Henceforth, benefitting from the boosted redox kinetics and the benignant electronic properties, the oxygen-deficient feature of LMO materials is conducive to ameliorating lithium diffusivity and intriguing pseudocapacitive-dominant behaviors, which is in uniformity with the pseudocapacitive observations and constitutionally interprets the oxygen vacancy-intervened electrochemical performances.

Additionally, a series of ex situ characterizations were conducted to further unearth the working mechanisms of the (O_v-)LMO during electrochemical measurements. It is widely substantiated that LMO materials undergo oxygen loss and generation of new spinel phases during cycling, resulting in inverted U-shaped cycling curves [17,47–49]. In brief, the severe phase transformation can cause intensified structural degradation and dissatisfying electrochemical performance. The ex situ XRD patterns of O_v-BDC-LMO (Fig. 8i) verify the phase transformation process as cycling proceeds, in which a negligible spinel trait can be detected before cycling and becomes more prominent after 50 and 100 cycles, indicating the formation of new spinel phases during repetitive delithiation/lithiation processes [46]. As expected, O_v-BTC-LMO (Fig. S22), O_v-PTC-LMO (Fig. S23), BDC-LMO (Fig. S24), BTC-LMO (Fig. S25), and PTC-LMO (Fig. S26) profoundly bear similar behaviors in local structure variations upon cycling, among which O_v-LMO samples show the suppressed structural change during cycling, while primitive LMO samples suffer from serious structural deterioration with the aggravated destruction of primitive layered structures. Hence, the significantly enhanced structural robustness of O_v-LMO originates from the alleviated phase attenuation and maintenance of the local structure.

Ex situ XPS spectra were employed to decipher the reaction mechanism during charge/discharge processes of (O_v-)LMO materials during the initial cycle, by which the exalted structural stability of O_v-LMO can be investigated from the perspective of electron status. As displayed in Fig. 8(j), Mn ions in O_v-BDC-LMO feature a mixed valence state of 3+ and 4+ during the initial discharge process from 2.4 to 4.7 V. After the discharge process to 2.5 V, Mn^{3+} ions were partially reduced to Mn^{2+}, corresponding to the subpeaks at 652.6 and 641.2 eV [60]. For a better comparison, the valence state of Mn in BDC-LMO was studied (Fig. S27), which elaborates the transformation from single (4+ before charging) to hybrid valence (4+/3+ and 4+/3+/2+ when charged to 4.7 V and discharged to 2.5 V, respectively) of Mn ions. These findings indicate the oxygen emission in primitive LMO during the first cycle coupled with the partial reduction of Mn^{4+} and transition metal (TM) layer change that facilitates the activation during the following cycles [17,48]. The electron status of oxygen for O_v-BDC-LMO during the charge/discharge processes was also unveiled by the core-level XPS spectra of O 1*s* at different charge/discharge states, as delivered in Fig. S28. The increasing intensity of O_2^{2-} when charged to 4.7 V can be ascribed to the oxygen shearing, while the obvious O^{2-} texture when discharged to 2.5 V reveals the recovery of lattice oxygen and the peculiar redox behavior of O_2^{2-}/O^{2-}. In contrast, BDC-LMO presented a drastically increasing O_2^{2-} feature when charged to 4.7 V and inferior O^{2-} recovery after the discharge process (Fig. S29). The different electron configurations of oxygen in O_v-BDC-LMO and BDC-LMO elucidate the relieved lattice oxygen loss, enhanced TM layer stability, and inhibited local structure destruction induced by the oxygen-deficient nature [49,53], thereby favoring the exalted electrochemical activity and extended cyclability.

3.3. DFT calculation results

DFT calculation was implemented to theoretically verify the superiority of the O_v-LMO materials in lithium storage compared with the parent materials. Herein, the models of LMO (Fig. 9a and Fig. S30a) and O_v-LMO (Fig. 9b and Fig. S30b) were established and optimized to further substantiate the amended crystalline

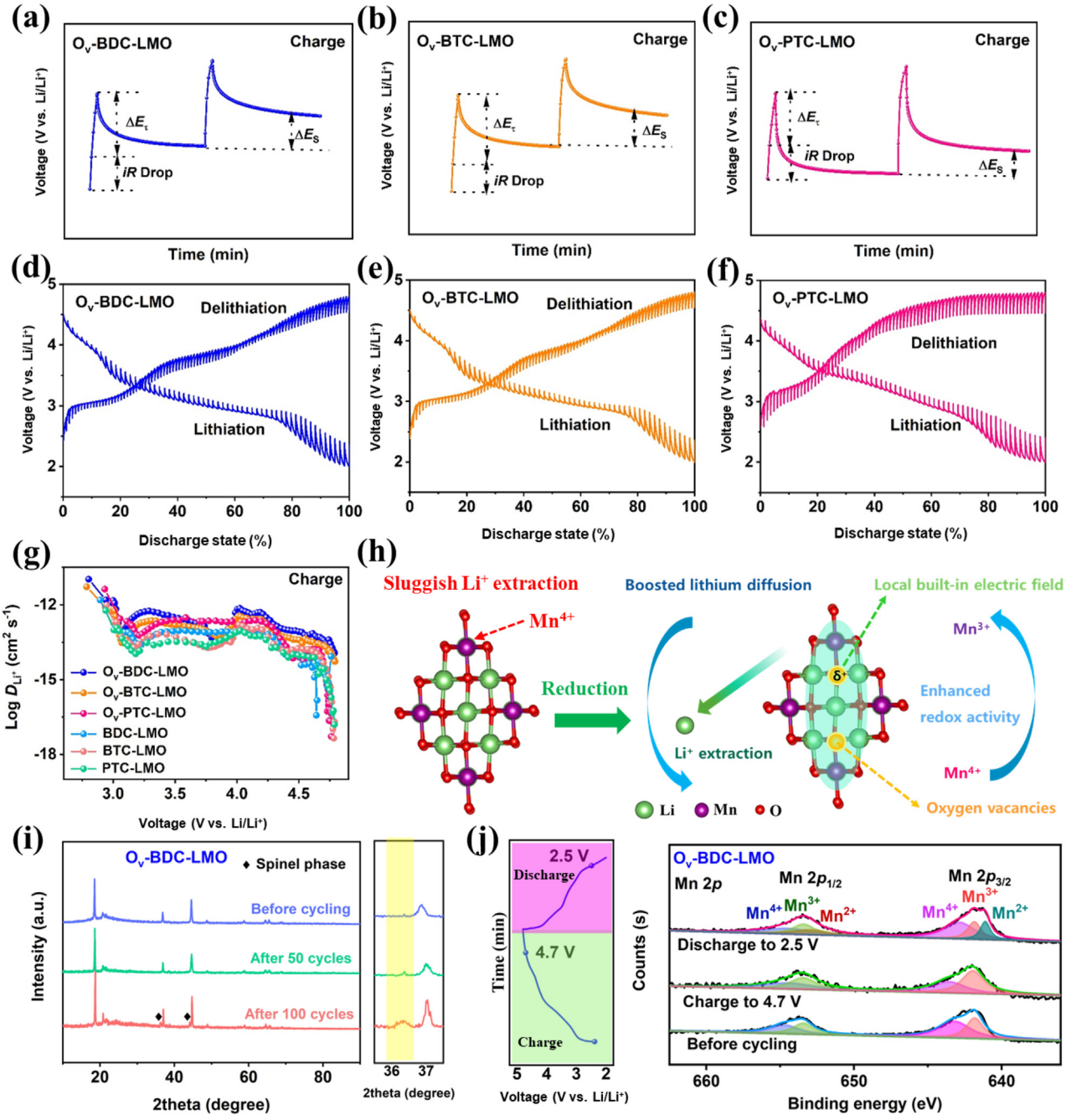

Fig. 8. The single-step profiles of GITT titration during the charging process for (a) O_v-BDC-LMO, (b) O_v-BTC-LMO, and (c) O_v-PTC-LMO. The GITT curves of (d) O_v-BDC-LMO, (e) O_v-BTC-LMO, and (f) O_v-PTC-LMO. (g) The calculated Li^+ diffusion coefficients upon charging for all samples. (h) The schematic illustration of the mechanism of boosted lithium diffusion for O_v-LMO samples. (i) Ex situ XRD patterns at different cycling states (before cycling, after 50 cycles, and after 100 cycles) and (j) Ex situ high-resolution XPS spectra at different charge/discharge states (before charging, charge to 4.7 V, and discharge to 2.5 V) of Mn 2*p* for O_v-BDC-LMO during the initial cycle.

configuration induced by oxygen vacancies. The calculated lattice parameters of LMO and O_v-LMO after optimization are enumerated in Table S5, which elucidates the enlarged lattice parameters and cell volume of the O_v-LMO. This result affirms the lattice expansion caused by the oxygen vacancy-induced atom occupancy variation [32], which is in agreement with the experimental findings.

To further unearth the difference in electronic configuration, the three-dimensional (3D) differential charge density distributions of LMO and O_v-LMO were explored, as presented in Fig. S30 (c) and Fig. 9(c), respectively. Visually, lopsided charge distribution can be observed around the oxygen vacancy site in the O_v-LMO, while there is no significant charge imbalance in the primitive LMO. These observations theoretically corroborate the feasibility and plausibility of the local built-in electric field assumption, thereby verifying the exalted lithium diffusivity related to the adventitious Coulomb force generated by the self-adaptive electric field around the vacancy area [34]. Consequently, it can be deduced that the charge accumulation around the oxygen defect sites elicits the auspicious electric force for expedited lithium ion transfer and unimpeded lithium storage reversibility.

Electronic conductivity is a crucial prerequisite condition for LIB electrodes, which was holistically investigated by calculating the total density of states (TDOS) profiles bound up with the Fermi level (denoted as E_f). As delivered in Fig. 9(d), both LMO and O_v-LMO exhibit semiconductive characteristics with apparent bandgap of 1.71 and 0.41 eV, respectively, between the valence

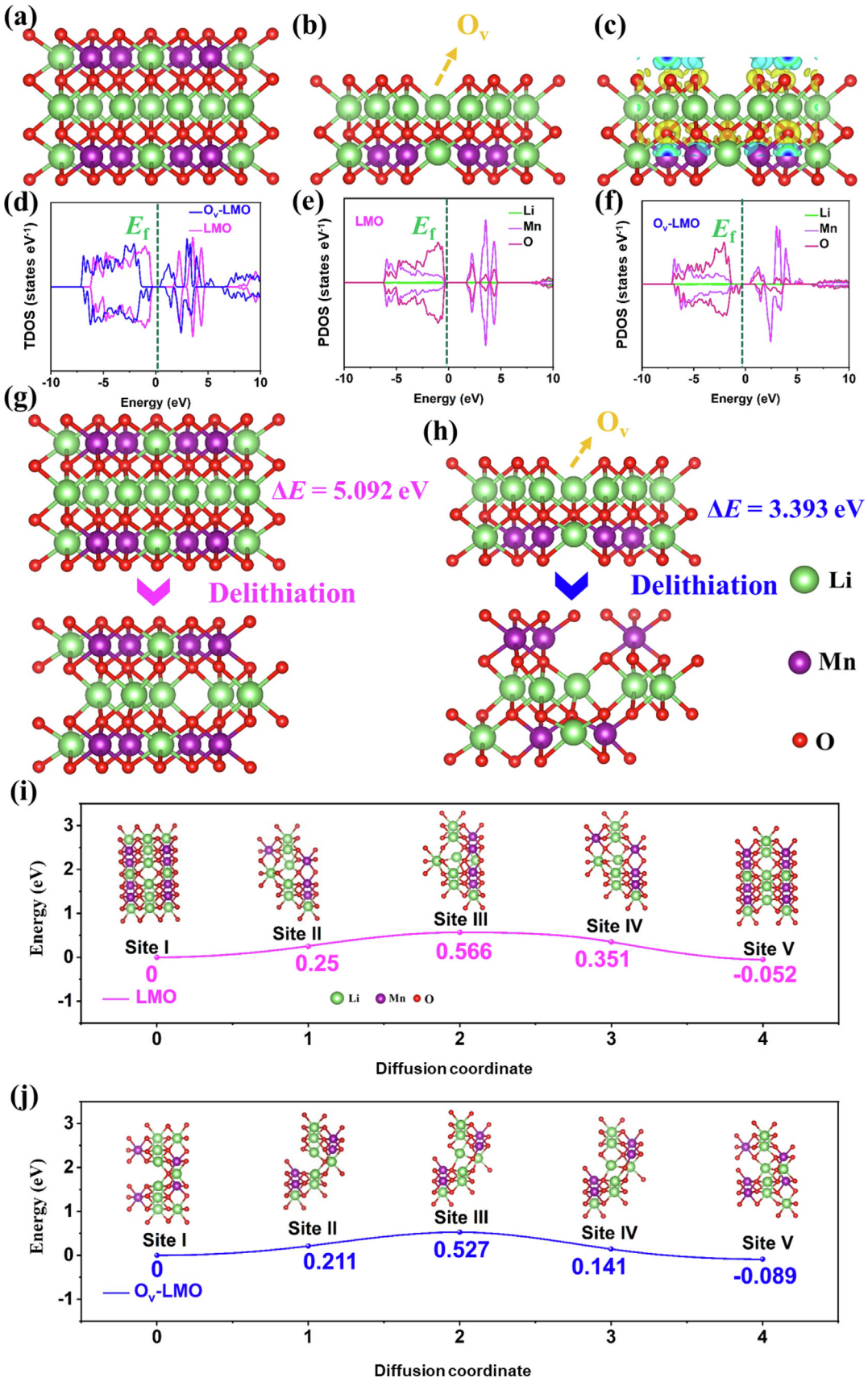

Fig. 9. The optimized models of (a) LMO and (b) O_v-LMO. (c) The 3D differential charge density distribution of O_v-LMO. (d) The TDOS curves of LMO and O_v-LMO. The PDOS curves of (e) LMO and (f) O_v-LMO. The energy barriers during delithiation for (g) LMO and (h) O_v-LMO. The lithium vacancy migration paths and corresponding energy barrier curves for (i) LMO and (j) O_v-LMO.

and conduction bands. The reduced band gap and pronouncedly denser DOS adjacent to the Fermi energy level delivered by the O_v-LMO indicate enhanced metallicity and impressive electronic conductivity. To further unravel the electronic states in detail, the partial density of states (PDOS) curves of LMO (Fig. 9e) and O_v-LMO (Fig. 9f) are calculated and compared. Noticeably, the 2*p* orbital of O and the 3*d* orbital of Mn appear closer to the vicinity of the valence band, indicating the prominently increased electron activity. This phenomenon can be ascribed to the facilitated excitation of the residual electrons around the oxygen-deficient region from the valence to the conduction band and the increased unpaired electrons in the Mn 3*d* orbital [32,61], which predominantly manipulates the electronic structure and elevates the electronic conductivity toward exceptional electrochemical performance.

As stated earlier, the ease of Li^+ extraction is vital to the reconstruction and activation of the LMO electrodes to sustain electrochemical activity, especially during the first cycle. To support this statement with more credible quantification, the Li^+ extraction process can also be more precisely evaluated by calculating the energy barriers during delithiation, which follows the relationship: $\Delta E = E_1 - E_2 + E_3$, where ΔE, E_1, E_2, and E_3 stand for the energy barrier during delithiation, energy after delithiation, energy before delithiation, and the energy of metallic Li utilized for calibration, respectively [62]. According to the relative energy at different states (Fig. S30d), the energy barriers upon delithiation of LMO (Fig. 9g) and O_v-LMO (Fig. 9h) can be mathematically determined to be 5.092 and 3.393 eV, respectively, uncovering the energetically favorable delithiation process triggered by oxygen defects.

The experimental observations extensively illuminate the significantly expedited Li^+ diffusion, which can be theoretically expounded by the calculated energy barriers of lithium vacancy migration. As displayed in Fig. 9(i), the relative energies at Sites I–V for LMO are 0, 0.25, 0.566, 0.351, and −0.052 eV, respectively. Meanwhile, the corresponding relative energies of 0, 0.211, 0.527, 0.141, and −0.089 eV at Sites I–V, respectively, for O_v-LMO are exhibited in Fig. 9(j). According to these findings, the minimum energy barriers for Li^+ diffusing to the neighboring Li vacancy in LMO (Fig. S31a) and O_v-LMO (Fig. S31b) can be determined to be 0.566 and 0.527 eV, respectively. This observation anticipates the accelerated lithium diffusion and fast Li^+ (de)intercalation kinetics in the oxygen vacancy-enriched lattice, which is endowed with expanded lattice space and extended pathways for ion migration and is adequately supported by experimental results.

Benefitting from the morphological and microstructural merits, the O_v-BDC-LMO reported in this study outperforms most of the counterparts mentioned in prior works in lithium storage capacity at various current densities, as depicted in Fig. S32. Taking the experimental and theoretical studies into account, the superiority in electrochemical properties of O_v-LMO is conferred by the following advantageous factors: (i) the enlarged lattice cell volume providing magnified space for Li^+ insertion and buffering volume variation; (ii) the modulated atomic arrangement and electronic configuration promoting ion/electronic conductivity; (iii) the energetically auspicious delithiation facilitating activation for the boosted redox activity and splendid reversible capacity; (iv) the expedited Li^+ transmission contributing to preponderant pseudocapacitive-dominant behaviors and extraordinary rate capability; (v) the rationally tailored morphology exposing more active sites and maximizing the electrode/electrolyte contact.

4. Conclusions

In conclusion, we have proposed a conceptual synthetic protocol with MOFs as self-sacrificial templates and stearic acid as the reductant for the introduction of oxygen vacancies to ameliorate the electrochemical activity of LMO as an advanced cathode material for LIBs. The rational selection of MOF precursors efficaciously modulates the morphological and structural properties of the LMO products, among which Mn-BDC-derived LMO materials outperform their counterparts due to the optimized morphology with smaller particle size, shortened diffusion aisles, increased active sites, and suppressed volume fluctuation. According to the experimental and theoretical findings, the successful introduction of oxygen vacancies facilitates the lithium storage activity of LMO materials with exalted reversible capacity, prolonged cycle life, and intriguing rate capability, which can be ascribed to the superior redox activity, alleviated structural degradation related to oxygen emission and phase transition, boosted electronic/ion conductivity, and extra pseudocapacitive contribution kinetically favoring lithium storage induced by the oxygen-deficient texture. This study envisions a versatile methodology to amend the morphological feature and electronic structure of LMO by integrating the MOF-templated method and oxygen-deficient strategy, which provides a new avenue to activate the LMO material for advanced lithium storage.

Declaration of competing interest

The authors declare that they have no known competing financial interests or personal relationships that could have appeared to influence the work reported in this paper.

Acknowledgments

We gratefully acknowledge the financial support from the Special Funds for the Cultivation of Guangdong College Students' Scientific and Technological Innovation ("Climbing Program" Special Funds, pdjh2023b0145), the Research and Development Plan Project in Key Fields of Guangdong Province (2020B0101030005), the Applied special project of Guangdong Provincial Science and Technology Plan (2017B090917002), and the Basic and Applied Basic Research Fund of Guangdong Province (2019B1515120027). Furthermore, the authors would like to thank the Shiyanjia lab (https://www.shiyanjia.com) for the TEM test.

Appendix A. Supplementary material

Supplementary data to this article can be found online at https://doi.org/10.1016/j.jechem.2023.05.014.

References

[1] R. Liu, N. Li, E. Zhao, J. Zhao, L. Yang, W. Wang, H. Liu, C. Zeng, Mater. Futures 1 (2022).
[2] Z.H. Zhang, X.Y. Xie, H.X. Xie, X.K. Ding, J.X. Cui, C.Y. Liu, D. Luo, Z. Lin, Chin. J. Struct. Chem. 41 (2022) 2204061–2204067.
[3] C. Zheng, S. Tang, F. Wen, J. Peng, W. Yang, Z. Lv, Y. Wu, W. Tang, Z. Gong, Y. Yang, Mater. Futures 1 (2022).
[4] S. Wang, J. Liu, Q. Sun, J. Mater. Chem. A 5 (2017) 16936–16943.
[5] J. Lin, Y.-H. Sun, X. Lin, Nano Energy 91 (2022).
[6] F. Wang, Z. Chang, X. Wang, Y. Wang, B. Chen, Y. Zhu, Y. Wu, J. Mater. Chem. A 3 (2015) 4840–4845.
[7] M. Zhang, L. Qiu, Y. Sun, Y. Song, Z. Wu, Y. Liu, Z. Yang, Y. Liu, J. Zhang, B. Zhong, X. Guo, ACS. Appl. Mater. Interfaces 13 (2021) 40995–41003.
[8] B. Wu, Z. Lin, G. Zhang, D. Zhang, W. Zhang, G. Li, Y. Che, L. Chen, H. Wang, W. Li, M. Chen, G. Cao, Energy Storage Mater. 53 (2022) 212–221.
[9] F. Ning, H. Shang, B. Li, N. Jiang, R. Zou, D. Xia, Energy Storage Mater. 22 (2019) 113–119.
[10] W. Zhao, L. Xiong, Y. Xu, H. Li, Z. Ren, J. Power Sources 349 (2017) 11–17.
[11] S.F. Amalraj, D. Sharon, M. Talianker, C.M. Julien, L. Burlaka, R. Lavi, E. Zhecheva, B. Markovsky, E. Zinigrad, D. Kovacheva, R. Stoyanova, D. Aurbach, Electrochim. Acta 97 (2013) 259–270.
[12] Y. Shin, K.A. Persson, ACS. Appl. Mater. Interfaces 8 (2016) 25595–25602.
[13] A.S. Menon, D.O. Ojwang, T. Willhammar, V.K. Peterson, K. Edstrom, C.P. Gomez, W.R. Brant, ACS. Appl. Mater. Interfaces 12 (2020) 5939–5950.

[14] Y. Sun, M. Guo, S. Shu, D. Ding, C. Wang, Y. Zhang, J. Yan, Appl. Surf. Sci. 585 (2022).
[15] Y. Wu, Y. Li, J. Gao, Q. Zhang, SusMat 1 (2021) 66–87.
[16] R.C.K. Reddy, X. Lin, A. Zeb, C.Y. Su, Electrochem. Energ. Rev. 5 (2021) 312–347.
[17] J. Rana, M. Stan, R. Kloepsch, J. Li, G. Schumacher, E. Welter, I. Zizak, J. Banhart, M. Winter, Adv. Energy Mater. 4 (2014) 1300998.
[18] K. Hikima, Y. Hinuma, K. Shimizu, K. Suzuki, S. Taminato, M. Hirayama, T. Masuda, K. Tamura, R. Kanno, ACS. Appl. Mater. Interfaces 13 (2021) 7650–7663.
[19] K. Kubota, T. Kaneko, M. Hirayama, M. Yonemura, Y. Imanari, K. Nakane, R. Kanno, J. Power Sources 216 (2012) 249–255.
[20] X. Tan, R. Liu, C. Xie, Q. Shen, J. Power Sources 374 (2018) 134–141.
[21] Y. Sun, L. Zan, Y. Zhang, Appl. Surf. Sci. 483 (2019) 270–277.
[22] S. Yadav, S. Sharma, S. Dutta, A. Sharma, A. Adholeya, R.K. Sharma, Inorg. Chem. 59 (2020) 8334–8344.
[23] J.-E. Zhou, J. Chen, X. Zhang, A. Zeb, X. Lin, J. Energy Chem. 75 (2022) 216–228.
[24] G. Kresse, J. Furthmüller, Comput. Mater. Sci 6 (1996) 15–50.
[25] J.P. Perdew, K. Burke, M. Ernzerhof, Phys. Rev. Lett. 77 (1996) 3865–3868.
[26] P.E. Blochl, Phys. Rev. B: Condens. Matter 50 (1994) 17953–17979.
[27] S. Grimme, J. Antony, S. Ehrlich, H. Krieg, J. Chem. Phys. 132 (2010).
[28] J. Zheng, P. Yan, L. Estevez, C. Wang, J.G. Zhang, Nano Energy 49 (2018) 538–548.
[29] C. Yin, Z. Bao, H. Tan, H. Zhou, J. Li, Chem. Eng. J. 372 (2019) 408–419.
[30] A. Quesne-Turin, D. Flahaut, G. Salvato Vallverdu, L. Croguennec, J. Allouche, F. Weill, M. Ménétrier, I. Baraille, Appl. Surf. Sci. 542 (2021).
[31] M. Chen, D. Chen, Y. Liao, X. Zhong, W. Li, Y. Zhang, ACS. Appl. Mater. Interfaces 8 (2016) 4575–4584.
[32] G. Zhang, M. Chen, C. Li, B. Wu, J. Chen, W. Xiang, X. Wen, D. Zhang, G. Cao, W. Li, Chem. Eng. J. 443 (2022).
[33] P. Lanz, C. Villevieille, P. Novák, Electrochim. Acta 109 (2013) 426–432.
[34] Y. Liu, T. Zhou, Y. Zheng, Z. He, C. Xiao, W.K. Pang, W. Tong, Y. Zou, B. Pan, Z. Guo, Y. Xie, ACS Nano 11 (2017) 8519–8526.
[35] B. Qiu, M. Zhang, L. Wu, J. Wang, Y. Xia, D. Qian, H. Liu, S. Hy, Y. Chen, K. An, Y. Zhu, Z. Liu, Y.S. Meng, Nat. Commun. 7 (2016) 12108.
[36] A. Zhu, Q. Wang, Y. Zhang, Y. Zhang, X. He, K. Wu, H. Wu, Q. Wang, W. Cai, Y. Zhang, J. Energy Chem. 71 (2022) 384–391.
[37] Y. Wang, L. Feng, W. Fan, K.Y. Wang, X. Wang, X. Wang, K. Zhang, X. Zhang, F. Dai, D. Sun, H.C. Zhou, J. Am. Chem. Soc. 141 (2019) 6967–6975.
[38] L. Xiao, J. Xiao, X. Yu, P. Yan, J. Zheng, M. Engelhard, P. Bhattacharya, C. Wang, X.-Q. Yang, J.-G. Zhang, Nano Energy 16 (2015) 143–151.
[39] J.-E. Zhou, J. Chen, Y. Peng, Y. Zheng, A. Zeb, X. Lin, Coord. Chem. Rev. 472 (2022).
[40] S. Cheng, Q. Ru, Y. Gao, M. Zhen, F. Chen, L. Wei, F.-C.-C. Ling, Chem. Eng. J. 406 (2021).
[41] A.P. Chernyshev, Mater. Chem. Phys. 282 (2022).
[42] M. Choi, W. Lee, Chem. Eng. J. 431 (2022).
[43] R. Jia, J. Yue, Q. Xia, J. Xu, X. Zhu, S. Sun, T. Zhai, H. Xia, Energy Storage Mater. 13 (2018) 303–311.
[44] C.R. Fell, D. Qian, K.J. Carroll, M. Chi, J.L. Jones, Y.S. Meng, Chem. Mater. 25 (2013) 1621–1629.
[45] Y. Zhang, C. Yin, B. Qiu, G. Chen, Y. Shang, Z. Liu, Energy Storage Mater. 53 (2022) 763–773.
[46] R. Wang, X. He, L. He, F. Wang, R. Xiao, L. Gu, H. Li, L. Chen, Adv. Energy Mater. 3 (2013) 1358–1367.
[47] P.J. Phillips, J. Bareño, Y. Li, D.P. Abraham, R.F. Klie, Adv. Energy Mater. 5 (2015) 1501252.
[48] D. Ye, G. Zeng, K. Nogita, K. Ozawa, M. Hankel, D.J. Searles, L. Wang, Adv. Funct. Mater. 25 (2015) 7488–7496.
[49] P. Yan, L. Xiao, J. Zheng, Y. Zhou, Y. He, X. Zu, S.X. Mao, J. Xiao, F. Gao, J.-G. Zhang, C.-M. Wang, Chem. Mater. 27 (2015) 975–982.
[50] C.O. Ehi-Eromosele, S.O. Ajayi, C.N. Onwucha, Mater. Chem. Phys. 259 (2021).
[51] M. Cheng, K. Zhu, L. Yang, L. Zhu, Y. Li, W. Tang, J. Alloys Compd. 686 (2016) 496–502.
[52] J. Lin, C. Zeng, Y. Chen, X. Lin, C. Xu, C. Su, J. Mater. Chem. A 8 (2020) 6607–6618.
[53] F. Li, X. Zhang, J. Lin, J. Ma, S. Zhang, G. Yang, J. Phys. Chem. C 123 (2019) 23403–23409.
[54] A. Klein, P. Axmann, C. Yada, M. Wohlfahrt-Mehrens, J. Power Sources 288 (2015) 302–307.
[55] J.-M. Savéant, ACS Catal. 8 (2018) 7608–7611.
[56] X. Zhang, J. Li, J. Li, L. Han, T. Lu, X. Zhang, G. Zhu, L. Pan, Chem. Eng. J. 385 (2020).
[57] Y. Hao, W. Liu, Q. Zhang, X. Wang, H. Yang, L. Kou, Z. Tian, L. Shao, H. Maleki Kheimeh Sari, J. Wang, H. Shan, X. Li, Nano Energy 88 (2021).
[58] X. Huang, J. Zhao, W. Zhu, M. Hou, T. Zhou, L. Bu, L. Gao, W. Zhang, J. Energy Chem. 63 (2021) 376–384.
[59] J. Yang, J. Xian, Q. Liu, Y. Sun, G. Li, J. Energy Chem. 69 (2022) 524–530.
[60] J. Lin, T. Huang, M. Lu, X. Lin, R.C.K. Reddy, X. Xu, Chem. Eng. J. 433 (2022).
[61] Q. Li, Y. Zhao, H. Liu, P. Xu, L. Yang, K. Pei, Q. Zeng, Y. Feng, P. Wang, R. Che, ACS Nano 13 (2019) (1934) 11921–11931.
[62] M.A. Kebede, M.J. Phasha, N. Kunjuzwa, L.J. le Roux, D. Mkhonto, K.I. Ozoemena, M.K. Mathe, Sustain. Energy Technol. Assess. 5 (2014) 44–49.